CALIFORNIA ENERGY COMMISSION

CALIFORNIA NATURAL RESOURCES AGENCY

Figure ENERGY RESEARCH AND DEVELOPMENT DIVISION

FINAL PROJECT REPORT

"Smart Greenhouse": Integrated Photovoltaics/Photosynthesis for Energy and Food

March 2024 | CEC-500-2024-017

PREPARED BY:

Prof. Yang Yang Dr. Yepin Zhao
Dr. Ying Zhang Mr. Jinsung Kim
Department of Materials Science and Engineering
University of California, Los Angeles
Primary Authors

Zack Bradford
Project Manager
California Energy Commission

Agreement Number: EPC-19-002

Anthony Ng
Branch Manager
Technology Innovation & Entrepreneurship Branch

Jonah Steinbuck, Ph.D.
Director
ENERGY RESEARCH AND DEVELOPMENT DIVISION

Drew Bohan
Executive Director

ACKNOWLEDGEMENTS

We thank the California Energy Commission (CEC) for the funding. We appreciate the help and consultation from the Commission Agreement Manager, Zack Bradford, and former managers, Katharina Gerber, Hassan Mohammed, and Baldomero Lasam. We thank Professor Yang Yang at UCLA for leadership and guidance.

PREFACE

The California Energy Commission's (CEC) Energy Research and Development Division supports energy research and development programs to spur innovation in energy efficiency, renewable energy and advanced clean generation, energy-related environmental protection, energy transmission, and distribution and transportation.

In 2012, the Electric Program Investment Charge (EPIC) was established by the California Public Utilities Commission to fund public investments in research to create and advance new energy solutions, foster regional innovation, and bring ideas from the lab to the marketplace. The EPIC Program is funded by California utility customers under the auspices of the California Public Utilities Commission. The CEC and the state's three largest investor-owned utilities—Pacific Gas and Electric Company, San Diego Gas and Electric Company, and Southern California Edison Company—were selected to administer the EPIC funds and advance novel technologies, tools, and strategies that provide benefits to their electric ratepayers.

The CEC is committed to ensuring public participation in its research and development programs that promote greater reliability, lower costs, and increase safety for the California electric ratepayer and include:

- Providing societal benefits.
- Reducing greenhouse gas emission in the electricity sector at the lowest possible cost.
- Supporting California's loading order to meet energy needs first with energy efficiency and demand response, next with renewable energy (distributed generation and utility scale), and finally with clean, conventional electricity supply.
- Supporting low-emission vehicles and transportation.
- Providing economic development.
- Using ratepayer funds efficiently.

For more information about the Energy Research and Development Division, please visit the CEC's research website (www.energy.ca.gov/research/) or contact the Energy Research and Development Division at ERDD@energy.ca.gov.

ABSTRACT

This project aims to help address food and energy demand in California and benefit California ratepayers by integrating photovoltaics into the food production system through greenhouses. The major goals of the project were to enhance the power conversion efficiency and transparency of organic solar cells and replace a greenhouse roof with semitransparent organic solar cells. To achieve these goals, the project pursued multiple strategies, including designing new materials for active layers of the solar cells, developing electrode and interfacial layers, and improving stability of the solar cells. During the project, the power conversion efficiency of the semitransparent organic solar cells achieved over 13.5 percent and the average visible transmittance achieved over 22 percent. The project team also successfully integrated semitransparent organic solar panels into a model power-generating greenhouse

Keywords: Organic photovoltaics, semi-transparent photovoltaics, smart greenhouse, organic semiconductors

Please use the following citation for this report:

Yang, Yang, Ying Zhang, Yepin Zhao, and Jinsung Kim. 2023. *"Smart Greenhouse": Integrated Photovoltaics/Photosynthesis for Energy and Food.* California Energy Commission. Publication Number: CEC-500-2024-017.

TABLE OF CONTENTS

LIST OF FIGURES

LIST OF TABLES

Executive Summary

Background

Sustainable management of food, energy, and water will be one of the strongest determinants of global human and environmental development over the coming century. California can contribute to advances in sustainable food, energy, and water by leveraging the state's dominant agricultural industry to demonstrate healthy soil and water conservation practices, effective pollution controls, and renewable energy generation. California is a leader in climate and clean energy policy with goals of 100 percent zero-carbon electricity sales and economy-wide net-zero greenhouse gas emissions by 2045. To meet these clean energy targets, a rapid expansion of clean electricity generation capacity is required. A "smart greenhouse", an advanced and automated agricultural facility designed to optimize the growth of plants and crops within a controlled environment, can generate clean electricity from a source that is currently underutilized, helping decarbonize agricultural operations while reducing resource consumption compared to traditional open-field farming.

In the past two decades, photovoltaic devices have significantly contributed to the rise in renewable electricity generation. Integrating photovoltaics into buildings and other structures such as greenhouses may further increase the capacity for renewable energy generation; however, there are several challenges to overcome, particularly for photovoltaic-integrated greenhouses. For example, opaque (or non-transparent) crystalline silicon photovoltaics mounted on greenhouse roofs block light and decrease crop production yields. Fresnel lenses, or concentric rings of prisms embedded in greenhouse roofs that focus light rays towards one location require costly and complex tracking equipment. A potential solution to these challenges may be mounting semitransparent photovoltaic modules onto the roofs and walls of greenhouses to allow solar radiation to pass through without the need for complex equipment. With the right materials, the wavelengths favorable to plant species can pass through the photovoltaics to allow for crop growth, while other wavelengths of light are harnessed by the photovoltaics for electricity generation. Forty-seven percent of the energy in sunlight is occupied by visible light, while the remaining 2 percent and 51percent are ultraviolet and infrared light, respectively. This means that infrared light has the greatest potential for energy supply; thus, semitransparent photovoltaic devices installed on greenhouses as roofs or windows, which utilize infrared light but allow for transmission of visible light, can be a promising solution to supply energy while growing food.

Organic photovoltaics may be strong contenders for applications such as photovoltaic windows, vehicle-integrated photovoltaics, and portable power supplies. In particular, the narrow band structure of organic semiconductors, as well as the photoactive layer thickness of organic solar cells makes them more competitive for building-integrated photovoltaic applications. The efficiencies of organic photovoltaics have seen great progress over the past several years, increasing in efficiency from less than 7 percent to 15-16 percent in under a decade for small devices for Average Visible Transparency, a key parameter that evaluates the transmittance of visible light. However, the efficiencies of organic photovoltaics still lag behind that of opaque

counterparts, due to the need to innovate materials, the design of novel and high-performance conducting electrodes with high optical transparency and electrical conductivity, and optical modeling. To promote highly efficient organic photovoltaics, efforts should be devoted to transparent top electrodes, optimal material selection, and balancing the inherent tradeoff between efficiency and Average Visible Transparency.

Project Purpose and Approach

The sun is an enormous and essentially "free" primary source of energy. However, a major challenge is to efficiently capture and convert it into a useful form of energy for human use. In the past two decades, photovoltaic devices have become a formidable solution to generate electricity. Generally, it is preferred that an ideal light-harvesting layer in photovoltaic devices absorbs most of the photons in the infrared region of the solar spectrum, while allowing those in the visible range of the spectrum to be transmitted. Inorganic semiconductors, however, cannot satisfy this requirement because they typically exhibit broad band-absorption. Interestingly, infrared-absorbing organic semiconductors with narrow bandgaps have shown great potential for both infrared-absorption and visible light transparency because their absorption spectrum can be tuned to localize in the infrared region instead of spreading over the entire spectrum. Tuning the absorption range of these organic semiconductors is achieved through novel chemical design and bandgap engineering. Moreover, solution-based processing provides the possibility of fabricating these organic materials on flexible substrates and over large areas with relatively simple equipment and at low costs.

The steady improvements in power conversion efficiency of visible light transparent organic photovoltaic devices to over 10 percent were achieved by a combination of material development and morphology optimization. The ranges of the spectrum that drive photosynthesis are highest in the red range of 600-700 nm, followed by the visible range of 400-600 nm. Most importantly, in the dominant range of 400-550 nm for photosynthetic processes, infrared-absorbing organic semiconductors demonstrate excellent transmittance, making them a superb choice for agricultural applications.

The project team aimed to achieve two major goals. The first goal was to improve the efficiency of organic photovoltaics to rival similar photovoltaic technologies. Through careful design of materials and advanced architectures, built upon a strong foundation and fundamental understanding of organic photovoltaics, the project team aimed to develop a champion organic photovoltaic that could achieve an efficiency greater than 15 percent and an Average Visible Transparency of 30 percent, which indicates that the solar cell is semi-transparent, allowing some natural light to pass through while generating electricity. For building-integrated photovoltaics and solar windows, transparency is essential in order to avoid obstructing views or reducing indoor illumination. The second goal was to prove the effectiveness of the "champion organic photovoltaic" (the most suitable organic photovoltaics for the greenhouses) when installed on the roof and windows of a model "smart greenhouse". A smart greenhouse is an advanced and automated agricultural facility designed to optimize the growth of plants and crops within a controlled environment, which allows for year-round cultivation, improved crop quality, increased yields, and reduced resource consumption compared to traditional open-field farming. By incorporating organic photovoltaics, smart greenhouses can become

more sustainable and energy efficient. The electricity generated by the organic solar cells can be used to power various systems within the greenhouse, such as climate control, irrigation, lighting, and data monitoring, reducing the reliance on external energy sources. The project planned to achieve these goals through five objectives:

- Objective 1: Design and manufacture new infrared absorbing donor and acceptor organic semiconductors.
- Objective 2: Design and manufacture advanced electrodes with a thickness less than 100 nanometers.
- Objective 3: Optimize interfacial layers in transparent organic photovoltaics.
- Objective 4: Manufacture transparent organic photovoltaic devices.
- Objective 5: Build and test miniaturized prototypes of "smart greenhouses" with integrated solution-processed 16 cm^2 and 120 cm^2 transparent organic photovoltaic devices and measure efficiency, transmittance, stability, reliability, and effects on plant growth.

Key Results

Design New Infrared Photovoltaic Materials

This project demonstrated effective strategies to successfully synthesize novel infrared materials. The project team demonstrated both donor and acceptor materials with absorption in the infrared light region and demonstrated an efficiency of 10.16 percent with an open-circuit voltage of 0.92 volts, a short circuit current of 15.79 mA/cm^2 and a fill factor of 69.95 percent. (Fill factor of solar cell: the ratio of maximum obtainable power to the product of the open-circuit voltage and short-circuit current.) This innovation has the potential to bring about numerous advantages for stakeholders, ranging from reduced energy costs and enhanced building aesthetics to environmental sustainability and job creation in the renewable energy sector.

Design and Manufacture Advanced Electrodes with a Thickness of Less Than 100 Nanometers

The project team designed and manufactured advanced electrodes with a reduced thickness by employing a conducting intermediate layer of poly (3,4-ethylenedioxythiophene) polystyrene sulfonate (PEDOT:PSS) between the hole selective layer and the electrodes. As a result, the project team saw a significant enhancement of the device's short circuit current, reaching a value close to that of opaque organic solar cells.

Interfacial Layer Optimization in Transparent Organic Photovoltaics

The project team developed a powerful reductive interlayer based on L-glutathione reduced for the transparent organic photovoltaic devices. The efficiency of the semitransparent device increased from 11.6 percent to 13.5 percent with an enhancement in short circuit current from 20.5 to 22.2 mA/cm^2, and plant growth in the organic photovoltaic-integrated greenhouse

achieved values comparable to that of a traditional glass-roof greenhouse. These results reinforced the feasibility of organic photovoltaics in agricultural applications. Furthermore, the improved stability suggests enhanced product reliability, product competitiveness, and reduced production cost, which may translate to reduced costs for California ratepayers.

Build and Test Miniaturized Prototypes of "Smart Greenhouses"

The project team used transparent plexiglass sheets (from Sosco Metals) to build model greenhouses. The team then tested semitransparent organic solar photovoltaic panels, opaque organic solar photovoltaic panels, segmented inorganic solar photovoltaic panels, and transparent panels on the model greenhouses. Each greenhouse roof was 30 cm in length and 15 cm in width, angled at 45 degrees. The results showed that the integration of the organic photovoltaics on the greenhouse roof did not impair plant growth because of the light absorption by the organic photovoltaics, and in fact, protected plants from detrimental ultraviolet exposure.

Knowledge Transfer and Next Steps

The findings and knowledge gained from this project were published in prestigious journals including *Nature Sustainability, Advanced Materials*, and *Advanced Energy Materials*, with over 300 citations. Local and nationwide media, such as Optics & Photonics News, Tech Xplore, Scinexx, Gizmag Emerging Technology Magazine, and Interesting Engineering, also reported on the project's achievements. A California company, Horizon PV, was founded and utilized the technology to serve local farmers and ratepayers with power-generating greenhouses near Los Angeles.

For next steps in the field of transparent organic photovoltaics, the project team recommends increasing investments in research and development (like production lines of the panels and mass production of the organic materials), enhancing regulatory support, and facilitating collaboration and partnerships between the solar industry and the architectural community for technology integration. The project team recommends reaching out to multiple potential investors in California, such as capital companies and large solar cell companies in Los Angeles and the Bay Area, to collaborate on next steps in the development of transparent organic solar cells. In conclusion, the broader adoption of semitransparent organic solar photovoltaic cells can significantly contribute to sustainable energy generation, green building practices, and reduced environmental impact. Informed policy and planning, along with supportive measures, are crucial to realizing the full potential of this technology.

CHAPTER 1: Introduction

Global food and energy security are dependent on fossil fuels as a principal raw material. Increasing amounts of renewable power generation will be needed to decarbonize these sectors to meet state, national, and international clean energy goals. California is a leader in climate and clean energy policy with goals of 100 percent zero-carbon electricity sales and economy-wide net-zero greenhouse gas emissions by 2045. Transforming the energy system of the world's fifth-largest economy within the next two decades will not be easy but it is essential. To meet the state's clean energy targets, a rapid expansion of clean electricity generation capacity is required. "Smart greenhouse" systems not only support decarbonizing greenhouse operations by generating clean electricity, but also increase annual crop yield while reducing resource consumption compared to traditional open-field farming. Greenhouses are one of the most efficient ways to control plant-growing conditions to optimize temperature, moisture, and sunlight. The fine control of the environment prolongs the growing season and broadens the crop species regardless of outdoor weather (Akira & Cossu, 2019) (Waller et al., 2021). However, large-scale greenhouse operations consume significant amounts of energy for heating, cooling, artificial lighting, pumping, and ventilation. Therefore, it is desirable to create a self-powered system within the greenhouse to offset energy consumption – a "smart greenhouse". Various photovoltaic (PV) greenhouses were developed by integrating various configurations of PV panels onto the walls and roofs of the greenhouses by researchers in the field of photovoltaics. For example, opaque silicon PVs mounted on greenhouse roofs can cause light blockage that leads to decreased crop production yields. Fresnel lenses, or concentric rings of prisms embedded in greenhouse roofs that focus light rays towards one location, require costly and complex tracking equipment. A potential solution to these challenges may be mounting semitransparent PV modules onto the roofs and walls of greenhouses to allow solar radiation to pass through without the need for complex equipment. The wavelengths of light favorable to plant species are allowed to pass through for crop growth, while the remaining light is harnessed by PVs for electricity generation. Although these aspects show that transparent organic photovoltaics (TOPVs) may be suitable for greenhouse applications, there are remaining fundamental and technical challenges, such as selective absorption of the solar spectrum to maximize crop growth and sustainable electricity generation.

TOPVs are promising for sustainable electricity generation in greenhouse systems because their light absorption spectrum can be tuned to localize in the infrared (IR) region instead of over the entire spectrum. The absorption spectrum required for photosynthesis of plants is usually located within the region of 400 – 700 nanometers (nm). In a typical greenhouse (i.e., a mild intensity sunlight environment), for instance, 10 percent of the full intensity AM 1.5G (a measure of the standard solar spectrum used for testing and characterizing solar cells and photovoltaic devices; AM means air mass; AM 1.5G: 1.5 atmosphere thickness, corresponds to a solar zenith angle of. =48.2°) visible sunlight, is enough for the growth of plants (Chang et al., 2018). IR-absorbing organic semiconductors demonstrate excellent transmittance in the light region. Tuning the absorption range of TOPVs can be achieved through novel chemical

design and bandgap engineering. Recent research demonstrated a power conversion efficiency (PCE) (the ratio of electrical power produced from light received) of 9.1 percent and an average visible transmittance (AVT) of 40.1 percent by incorporating a near-infrared (NIR) absorbing acceptor into a bulk heterojunction organic solar cell (Xie, 2020). Other research of non-fullerene organic small molecule acceptors pushed the PCE of TOPVs to 10 percent with an AVT of around 20 percent (Chen & Zhang, 2017) (Liu et al., 2021). Along with spectrum tunability, TOPVs can be fabricated onto flexible substrates such as low-density polyethylene, the most commonly used polymer for greenhouses. As a result, this technology may reduce costs of building new PV greenhouses or retrofitting old ones with PV-covered roofs. Moreover, solution processability of TOPVs makes the device printable by roll-to-roll processing for large-areas in mass production. These cost-savings and ease of installation can benefit municipalities, local farm communities, and farmers.

The project team aimed to achieve two major goals. The first goal was to improve the efficiency of TOPVs to 15 percent with an AVT of 30 percent through molecular design of donor and acceptor active materials. The second goal was to demonstrate installation of TOPVs on roofs or windows of smart greenhouses. To achieve these goals, the team followed four approaches. (1) Require solution processed large-area TOPVs. Although the preliminary devices are 1 cm^2, a device area of 16 cm^2 at the first stage by blade-cast devices was achievable. (2) Adopt acceptors with enhanced photochemical stability for further stabilization of "smart greenhouses". (3) Establish a database of high-performance TOPV systems and agronomic preferences with the specific solar spectrum. (4) Construct an integrated system, including an inverter, as a test module for large-scale commercialization. To verify the potential for plant growth, the team measured lengths, length deviations, biomass productivities, leaf area, and survival rates of plants grown within the model greenhouses. The results for the semitransparent greenhouses were compared to greenhouses with segmented inorganic solar cells.

CHAPTER 2:
Project Approach

Technology/Research Objectives

The main goal of this project was to manufacture 4 cm x 4 cm organic photovoltaic (OPV) devices with a PCE approaching or exceeding 15 percent and an AVT approaching or exceeding 30 percent. This was accomplished through the following specific objectives:

- Design and manufacture new IR absorbing donor and acceptor organic semiconductors.
- Design and manufacture advanced electrodes with a thickness <100 nm.
- Optimize interfacial layers in TOPVs.
- Manufacture TOPV devices.
- Build and test miniaturized prototypes (models) of "smart greenhouses" with integrated solution-processed 16 cm^2 and 120 cm^2 TOPV devices, and measure efficiency, transmittance, stability, reliability, and effect on plant growth.

Project Partners, Advisors, and Other Project Participants

The project leader was Professor Yang Yang, the Tannas Jr. Chair Professor at the University of California, Los Angeles (UCLA). The project participants were Dr. Yepin Zhao, postdoctoral researcher at UCLA, Dr. Ying Zhang, postdoctoral researcher at UCLA, Dr. Dong Meng, postdoctoral researcher at UCLA, Wenxin Yang, Ph. D student at UCLA, and Jinsung Kim, Ph. D student at UCLA. The California Energy Commission Agreement Manager was Zack Bradford.

Overall Approach

Design and Manufacture New IR-Absorbing Donor and Acceptor Organic Semiconductors

The design and synthesis of IR-absorbing materials required fundamental understanding of molecular concepts to design the unique arrangement of emerging molecular building blocks, as well as experience and skill to synthesize and purify the materials (Figure 1, 2). The new materials needed superior solubility and a desired aggregation property for device fabrication. To broaden the absorption range of the polymers, the project team adopted alkoxy groups into the molecules to elevate the highest occupied molecular orbital (HOMO) while retaining the same or better solubility for device processability.

Initially, the project team incorporated an alkoxy group into the following polymer (Figure 1). However, the team found that the solubility was reduced, which was opposite from what was expected. The team found that the distribution of the solubilizing side-chain substituents in the polymer main chain should be appropriately considered, otherwise the aggregation and the

packing orientation would hinder solubility (Cheng & Yang, 2020) (Meng et al., 2021) (Cheng et al. 2022).

Figure 1: Structure of polymer PTOT2FBT

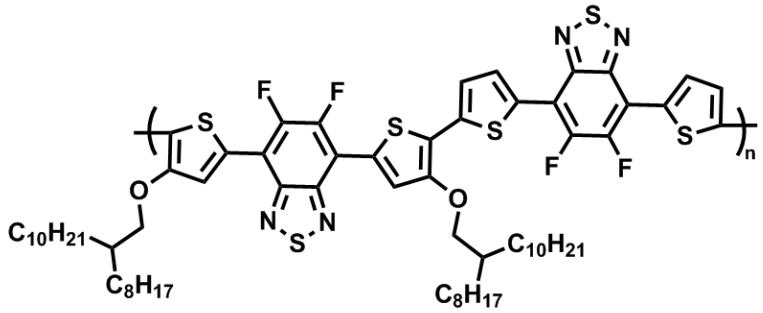

Source: UCLA

Figure 2: The Structure, Energy Level, and UV-vis-NIR Absorption Spectra of OTBO Series Polymers

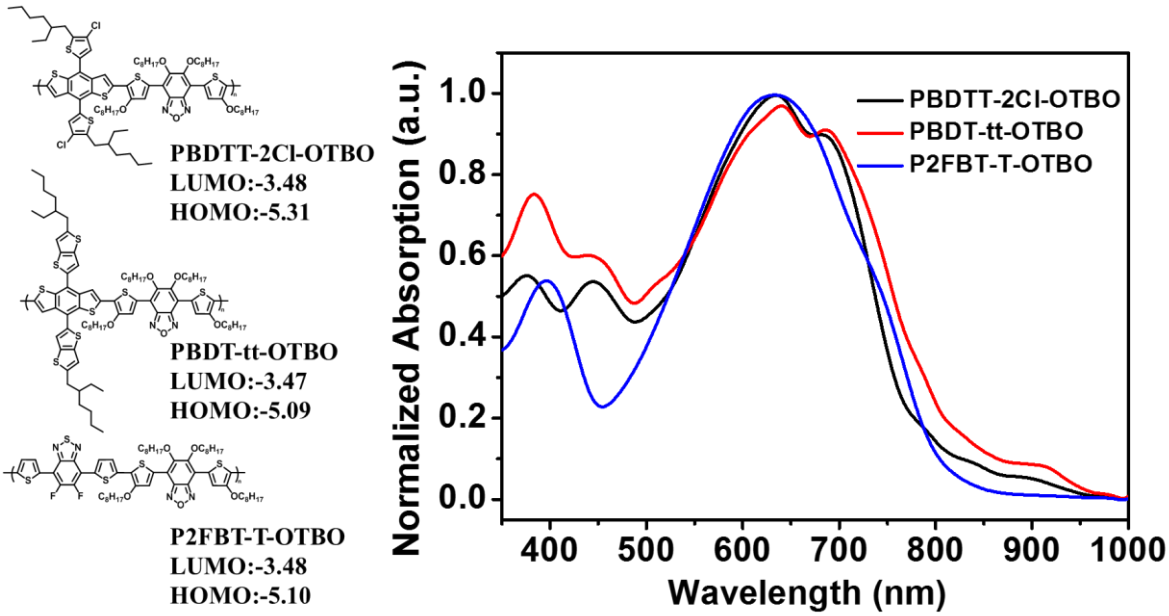

Source: UCLA

Subsequently, the team changed the distribution of the alkoxy chains so they can attach more evenly on the polymer main chain, which led to successful synthesis of those polymers. The incorporation of the alkoxy group to the pi (π) bridge of polymers can also increase the polymers' solubility, which could be a strategy for further optimization of the building block structure.

Finally, to entirely exclude the effects of the long alkyl chain, the team synthesized a series of polymers based on the incorporation of methoxy groups to the bithiophene unit to elevate more of the highest occupied molecular orbitals (HOMOs) than the lowest unoccupied

molecular orbitals (LUMOs) of the polymers, thereby narrowing the bandgap to the IR region (Figure 3, 4).

Figure 3: Structures of the Monomers M1–M3 and Synthetic Route to Copolymers P1–P5

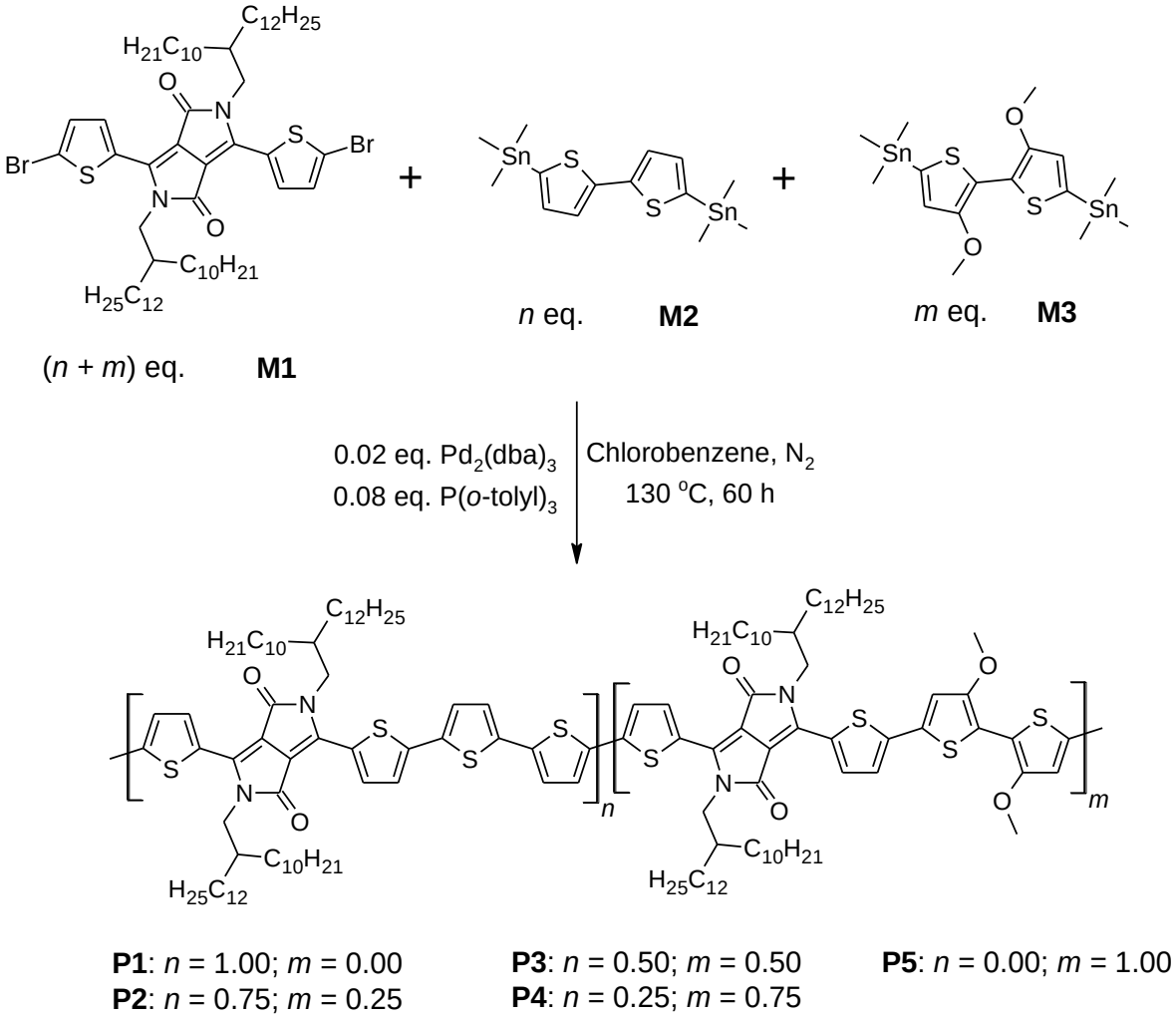

Source: UCLA

The team developed a new molecule, SFIC-Cl, using a biplanar conjugated cruciform-shaped spirobifluorene (SF) as the centroid core and 2-(5,6-dichloro-3-oxo-2,3-dihydro-1H-inden-1-ylidene) malononitrile (2Cl-IC) as a multijoint fragment connecting adjacent molecules. It features enhanced π-electron delocalization by spiro conjugation and narrowed bandgap by chlorination, which showed a PCE of 10.16 percent resulting from the broadened and strong absorption and well-matched energy levels. The study demonstrated that chlorinated spiro-conjugated fused systems offer a novel direction toward the development of high-performance organic semiconductor materials for TOPVs (Men et al., 2021).

The synthetic route to SFIC-Cl is shown in Figure 4. Compound (1) in Figure 4 was synthesized via four-fold Suzuki-Miyaura coupling reactions between 2-bromothiophene-3-carboxylate and 2,2',7,7'-tetrakis(pinacolatoboryl)- 9,9'-Spirobi[9H-fluorene] using Pd(PPh3)4 as a catalyst and

K2CO3 as a base in 80 percent yield (Figure 4). Quadruple nucleophilic addition of freshly prepared 4-(2-ethylhexyl) phenyl magnesium bromide to the ester groups of compound (1) led to the formation of benzylic alcohol ((2) in Figure 4) which was subjected to intramolecular annulation through acid-mediated Friedel–Crafts reaction to afford the fused double-hepta-cyclic arene ((3) in Figure 4). For the effective reaction, the project team used the organic acid boron trifluoride diethyl etherate and achieved a 75 percent yield. Subsequent compound (4) in Figure 4 was prepared by Vilsmeier–Haack reaction of compound (3) in Figure 4 using POCl3 and DMF (N,N-Dimethylformamide). The target product SFIC-Cl was obtained via Knoevenagel condensation between compound (4) and 2-(5,6-dichloro-3-oxo-2,3-dihydro-1H-inden-1-ylidene) malononitrile, resulting in 85 percent yield.

Figure 4: Synthetic Route to SFIC-Cl

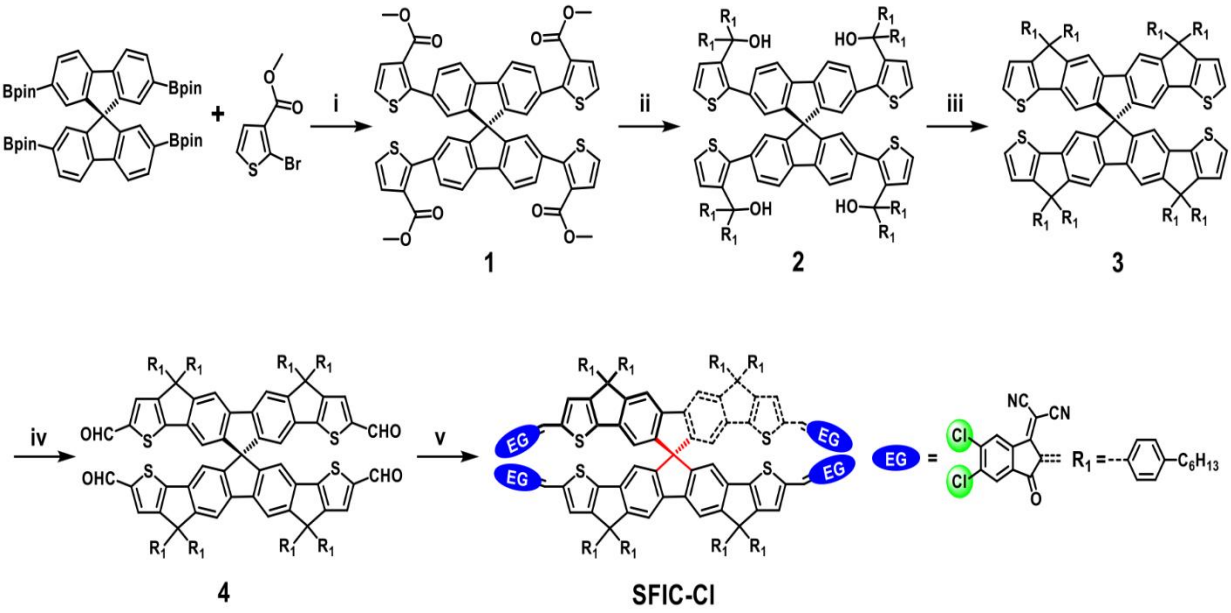

Source: UCLA

The reaction conditions were (i) Methyl 2-bromothiophene-3-carboxylate (4.5 equiv.), 2,2',7,7'-tetrakis(pinacolatoboryl)- 9,9'-Spirobi[*9H*-fluorene] (1.0 equiv), $Pd(PPh_3)_4$ (0.3 equiv), K_2CO_3 (2M)/THF (1:2), 95 °C, 72h. Yield: 80%. (ii) 1-bromo-4-hexylbenzene (22 equiv.), magnesium turnings (26.4 equiv.), THF, RT to 70 °C, 20 h. Yield: 85%. (iii) Boron trifluoride diethyl etherate (diluted by chloroform), chloroform, 70 °C, 24h. Yield: 75%. (iv) DMF, $POCl_3$, 0 °C to 90 °C, 20h. Yield: 70%. (v) 2-(5,6-dichloro-3-oxo-2,3-dihydro-1H-inden-1-ylidene) malononitrile (12 equiv.), pyridine (1 ml), chloroform, 70 °C**,** Yield: 85%.

Design and Manufacture Advanced Electrodes with a Thickness of <100 nm

The project team designed and manufactured advanced electrodes with reduced thickness by employing a conducting intermediate layer of poly (3,4-ethylenedioxythiophene) polystyrene sulfonate (PEDOT:PSS) between the hole selective layer (MoO_3 layer for common devices) and the electrodes (ultra-thin Ag (silver) layer for common devices) (Figure 5) (Zhao et al., 2021). During this stage of the experiment, the project team applied PCE10/POIC as the active layer

of the devices. A decrease in overall performance was observed as the devices were made semi-transparent as demonstrated by a large reduction in the short circuit current (J_{sc}) (the maximum current that can be extracted from the device at short circuit conditions). After applying the PEDOT:PSS modification between the MoO_3 layer and the ultra-thin Ag, a significant enhancement of the device J_{sc} was seen, which aligned closely with that of opaque devices.

Figure 5: Schematic Employment of Intermediate Layer of PEDOT:PSS between MoO_3 Layer and the Ultra-Thin Ag Layer

Source: UCLA

Optimize Interfacial Layers in TOPV

The project team developed a powerful reductive interlayer based on L-glutathione reduced (L-G, Figure 6a) for the TOPV devices with PM6/Y6 as the active layer. With the insertion of the interlayer, both PCE and J_{sc} of the semitransparent device increased (Figure 6c) (Zhao et al., 2023). The interface resistance was lowered and charge transfer between the ZnO layer and the PM6/Y6 active layer was facilitated. Additionally, due to the strong reducibility of the L-G molecule, the production of the superoxide radicals was significantly suppressed. After continuous illumination with 1-sun intensity for 15 days, the molecular structure and packing in the organic active layer remained almost unchanged, while the reference active layer showed great decomposition. Plant growth in the TOPV-integrated greenhouse was comparable to the traditional glass-roof greenhouse. These results reinforced the feasibility of the TOPVs in agricultural applications and other practical scenarios.

Figure 6: Enhanced charge extraction and photovoltaic performance with the incorporation of the L-Glutathione reduced interlayer (A) Molecular structures of L-Glutathione reduced and TOPV architecture with the L-Glutathione reduced interlayer. (B) J-V curves of the TOPVs based on PM6/Y6 with and without applying the L-Glutathione reduced interlayer

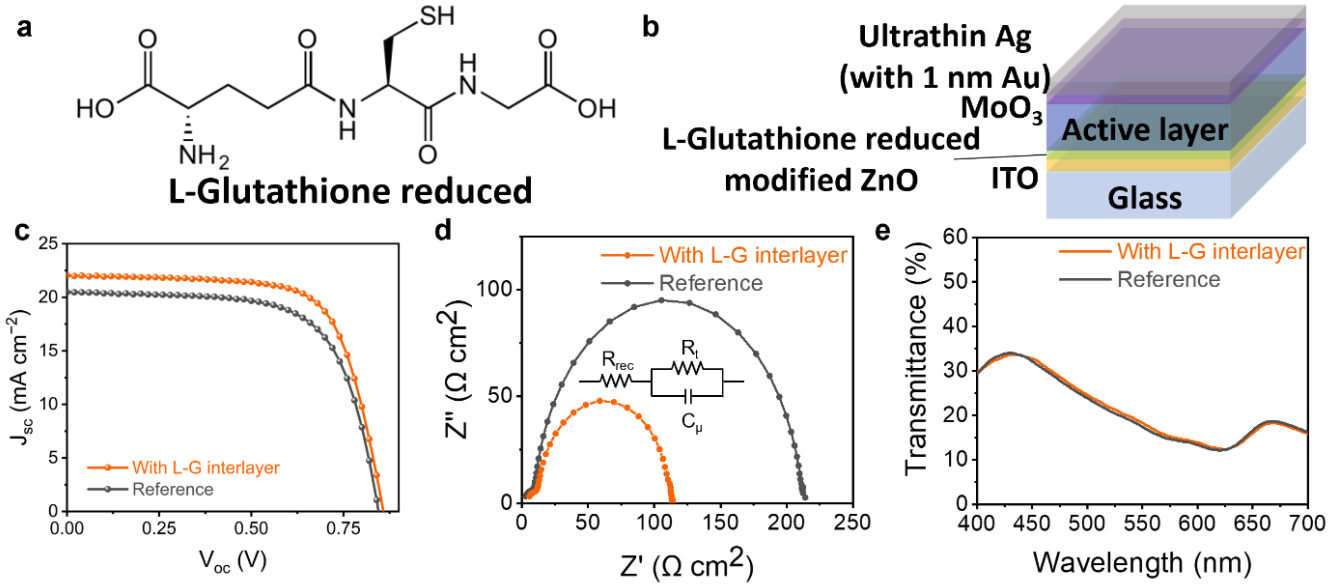

Source: UCLA

Build and test miniaturized prototypes of "smart greenhouses"

Transparent plexiglass sheets (from Sosco Metals) were used to build the model greenhouse prototypes, measuring 30 cm in length by 21.5 cm in width by 15 cm in height. Semitransparent organic solar panels, opaque organic solar panels, segmented inorganic solar panels, and transparent panels were each studied. Each greenhouse included two roofs with a length of 30 cm and a width of 15 cm, angled at 45 degrees. To ensure complete coverage of the solar cells for testing purposes, the walls of each greenhouse were covered by black tape and aluminum foil during plant growth. Rectangular polypropylene trays (from SHEING) with a length of 26.5 cm and a width of 19.5 cm were used to germinate the plants and were placed directly under the greenhouses. When verifying the influence of the UV light on the plant growth, an extra UV filter (from Edmund Optics) was added on top of the greenhouse roofs (Zhao et al., 2023).

Three types of commonly consumed plants, mung bean (*Vigna radiata*), wheat (*triticum aestivum*), and broccoli (*Brassica oleracea*) sprout, were chosen to evaluate growing conditions under the greenhouses with the various solar roofs. As the size of the seeds differed, the seed spacings were adjusted accordingly, at 0.2 count cm^{-2}, 0.3 count cm^{-2}, and 2.7 count cm^{-2} for mung bean, wheat, and broccoli sprouts, respectively. All seeds were immersed in water for 1 day before being placed evenly in a tray with water underneath. Then, each tray was loaded in a different greenhouse and placed outside for eight consecutive days. The experiments of each condition were repeated at least three times. The water temperature in the greenhouses was kept stable through hourly exchanges of fresh water (~20 °C) during the

day. The height of the plants was monitored daily at 6:00 p.m., together with water refilling to ensure the plants stayed hydrated. The length of the sprouts was measured based on the distance from the top to the bottom of the root. The area of the leaves was collected by removing the leaves and analyzing them using a photo analysis software tool called Image J. The plant survival rate was calculated by counting the number of surviving sprouts normalized by the number of initial seeds. All plants in the various greenhouses were counted and averaged for statistical analysis.

To evaluate the plant biomass production, the team measured the biomass of the different plants after eight days of growth in the greenhouses. Biomass was measured by summing the dry mass of all organics, including the surviving sprouts, the roots, dead sprouts, and ungerminated seeds. The biomass was placed in a 90°C oven for three days to remove excess water. The weight of each batch was measured using a balance, and the final weight was normalized based on their initial mass. The biomass productivity was calculated using the following equation:

$$P = (N_2 - N_1)/(t_2 - t_1)$$

where N_1 and N_2 are defined as the biomass at time 1 (t_1) and time 2 (t_2), respectively.

Global horizontal irradiance (GHI) is defined as the total solar radiation incident on a horizontal surface. It is the sum of diffuse horizontal irradiance, direct normal irradiance (DNI), and ground-reflected radiation. The GHI source used to evaluate the concurrent electricity production was provided by Solcast. According to the Solcast data source, local cloud covering was included to render a precise and accurate global snapshot of solar irradiance. The total energy power and the daily average power for each round of plant growth were calculated based on the GHI profile. Considering the performance loss during scaling up, we used 20 percent and 11 percent as the estimated power conversion efficiencies for inorganic solar cells and semitransparent solar cells, respectively. The electricity production for each greenhouse was calculated based on the roof panel size, the angle to the horizon, and the GHI profile.

Key Project Milestones

Key project milestones included conducting experiments on the rooftops and/or windows of a scaled-down "smart greenhouse" laboratory to harness solar energy while simultaneously enabling photosynthesis necessary for plant growth. Additionally, the project team established a protocol for evaluating the performance of these power-generating greenhouses.

CHAPTER 3:
Results

Technology and Research Outcomes

Led by the five specific objectives of this project as described above, the project team achieved several technology and research advances:

New IR Absorbing Donors and Acceptors

The project team applied "side chain engineering" to the pi-bridge of donor polymer materials. Alkoxy groups were adopted into the molecules to elevate the HOMO yet retain the same or better solubility for device processability. The absorption could be easily red-shifted to the IR region. To entirely exclude the effects of the long alkyl chain, the project team synthesized a series of polymers based on the incorporation of a methoxy group to the bithiophene unit to elevate more of the HOMOs than the LUMOs of the polymers, thereby narrowing the bandgap to the IR region (Figures 3, 7, Table 1).

Figure 7: UV-vis-NIR Absorption Spectra of Copolymers P1–P5

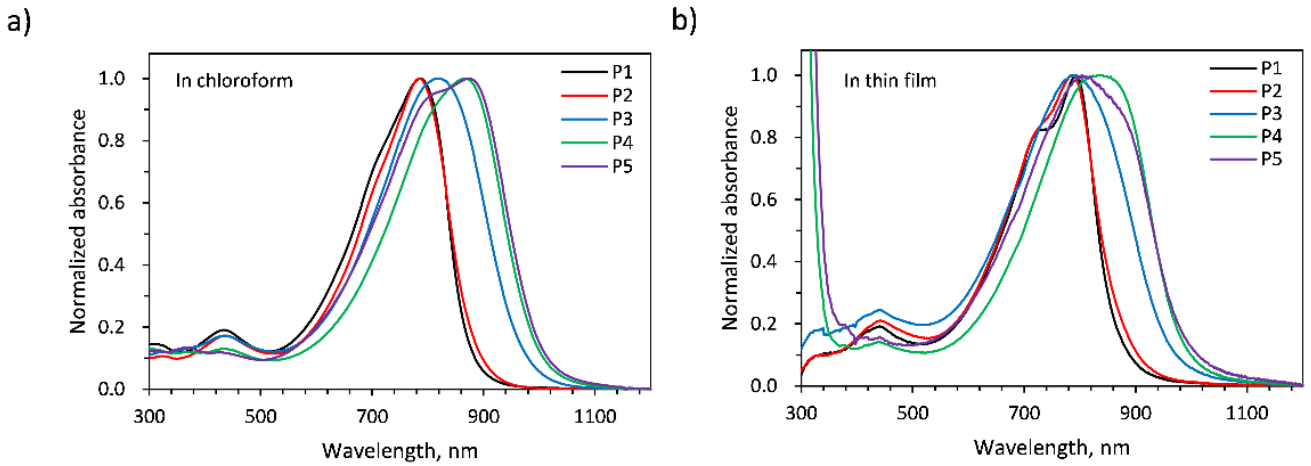

(a) in chloroform solutions and (b) in thin films

Source: UCLA

Table 1: Summary of Properties of P1–P5

Polymer	Mn, kg mol−1	PDI	Td, °C (a)	Eg,opt, eV (b)	EHOMO, eV (c)	ELUMO, eV (d)
P1	36.1	2.79	406	1.40	−5.30	−3.90
P2	64.4	4.81	412	1.39	−5.32	−3.93
P3	1.95	2.20	386	1.28	−5.17	−3.89

Polymer	Mn, kg mol−1	PDI	Td, °C (a)	Eg,opt, eV (b)	EHOMO, eV (c)	ELUMO, eV (d)
P4	2.59	1.83	384	1.25	−5.06	−3.81
P5	3.00	2.23	382	1.24	−4.86	−3.62

(a) Temperature corresponding to 5% weight loss. (b) Determined from the onset of absorption band in thin film. (c) Determined from the onset of the oxidation peak in cyclic voltammetry curve. (d) Calculated $E_{LUMO} = E_{HOMO} + E_{g,opt}$.

A new molecule, SFIC-Cl, was developed featuring enhanced π-electron delocalization by spiro conjugation and narrowed bandgap by chlorination, which showed a PCE of 10.16 percent resulting from the broadened and strong absorption and well-matched energy levels. The study demonstrated that chlorinated spiro-conjugated fused systems offer a novel direction toward the development of high-performance organic semiconductor materials for TOPVs.

The highest PCE was achieved for the optimized device with a donor/acceptor ratio of 1:1 and 0.5 volume percent of Chloronaphthalene. Figure 8B and 8C show the current density-voltage (J-V) curve and external quantum efficiency (EQE) spectrum of the champion OPV device under the illumination of an AM 1.5G solar simulator at 100 mW cm^{-2}. A PCE of 10.16 percent was realized with a V_{oc} of 0.92 V, a J_{sc} of 15.79 mA/cm^2, and a fill factor (FF) of 69.95 percent. In the wavelength range between 550 and 700 nm, the observed high EQE values of over 70 percent may be contributed from the strong absorption of the SFIC-Cl and PBDB-T-2Cl, which is consistent with the high J_{sc} obtained from the J-V measurement.

Figure 8: SFIC-Cl Based OPV Devices

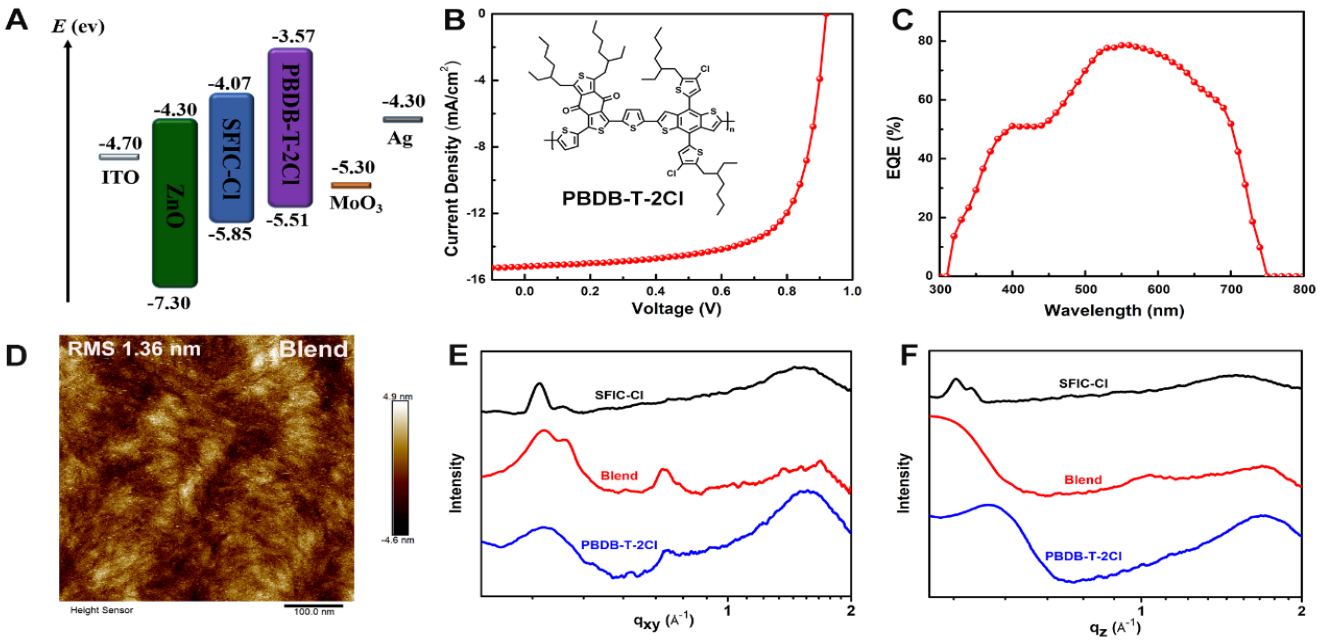

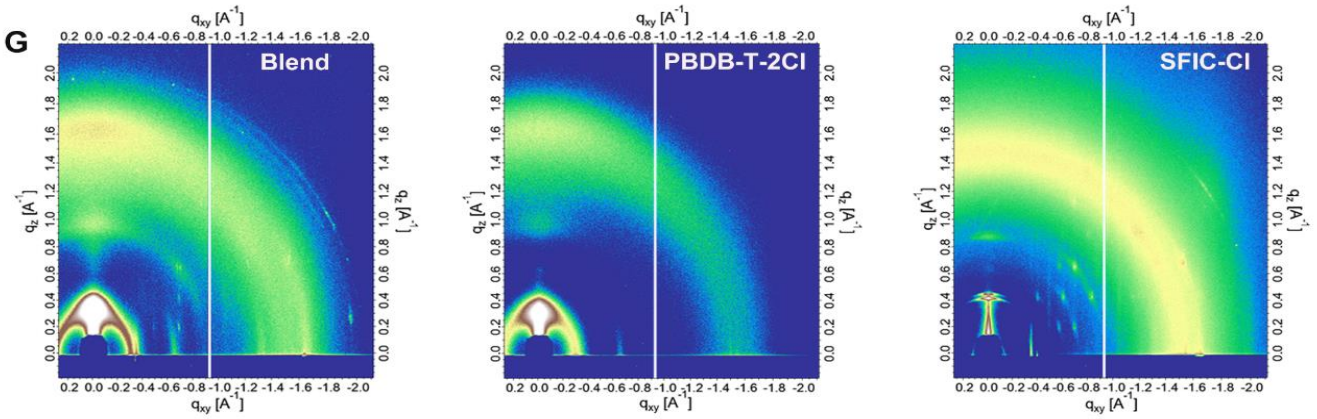

(A) Energy level diagram of every component applied in the device. (B) J-V curve (The inset is the chemical structure of PBDB-T-2Cl donor) and (C) EQE spectrum of the champion OPV device. (D) atomic force microscopy image of PBDB-T-2Cl/SFIC-Cl blend film. GIWAXS intensity line profiles along with in-plane direction (E) and out-of-plane direction (F). (G) 2D GIWAXS images of PBDB-T-2Cl/SFIC-Cl blend film, PBDB-T-2Cl and SFIC-Cl neat films.

Source: UCLA

To gain further insight into the high performance of the OPV device, the project team characterized the surface morphology and molecular packing behavior of the active layer using atomic force microscopy (AFM) and two-dimensional grazing incident wide angle X-Ray scattering (2D-GIWAXS).

Further, the project team tried to enhance the performance of the TOPVs by changing the component of the active layer. The team successfully developed an employed "transparent hole transporting frameworks" strategy to increase the PCE of the device, while maintaining its average visible transmittance (AVT) (Cheng et al., 2020). The employed "transparent hole transporting frameworks" strategy is shown in Figure 9. A hole-transporting large band gap polymer (poly[bis(4-phenyl) (2,4,6-trimethylphenyl) amine (PTAA)) was employed to partially replace the polymer donors in the active layer of polymer donor (PBDB-T with a bandgap of 1.8 eV) and nonfullerene acceptor (Y1 with a bandgap of 1.4 eV). Considering PTAA is a p-type polymer with a large bandgap of 2.9 eV, the partial substitution of PBDB-T by PTAA may reduce the absorption of the active layer only in the visible region, maintaining the hole-transporting pathways as well as the optimized film morphology (just like transparent hole-transporting frameworks, Figure 9a).

Figure 9: a) Schematic diagrams of active layers without or with PTAA. b) Molecular structures of donor (PBDB-T), acceptor (Y1), and PTAA. c) Energy levels of PBDB-T, Y1, and PTAA as well as the proposed charge transfer/charge transport

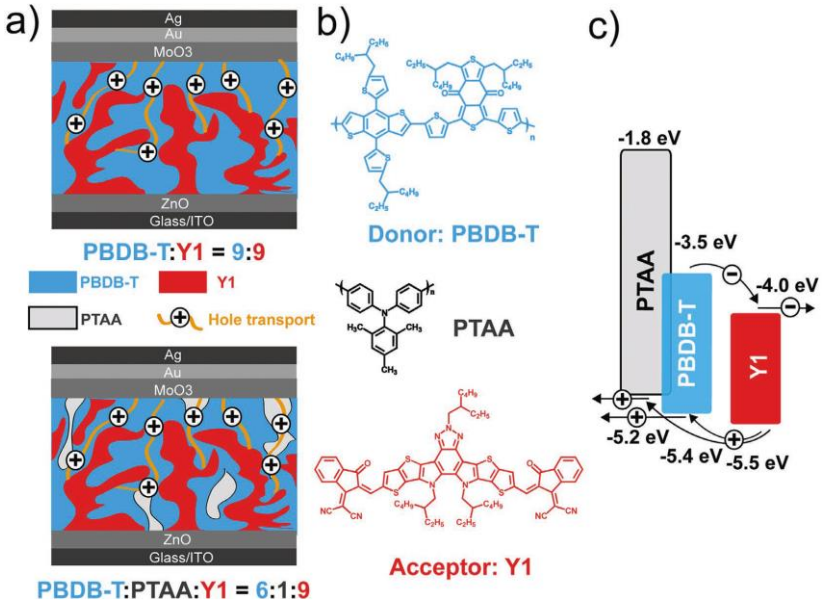

Source: UCLA

The molecular structures of donor (PBDB-T), PTAA, and acceptor (Y1) are shown in Figure 9b. The absorption spectra of donor (PBDB-T), PTAA, and acceptor (Y1) are shown in Figure 10a. Energy levels of PBDB-T, PTAA, and Y1 as well as the proposed charge transfer/charge transport are shown in Figure 10c. By partial substitution of the donor by PTAA, the excitons generated by the acceptors can be dissociated at both donor/acceptor and PTAA/acceptor interfaces. Afterward, the holes can be transported by both the donor and PTAA. The absorption spectra of the PBDB-T/Y1 9:9 (i.e., w/o), PBDB-T/PTAA/Y1 6:1:9 (i.e., w/ PTAA) and the PBDB-T/Y1 6:9 films are shown in Figure 10b, which indicate that the partial substitution of PBDB-T by PTAA sufficiently reduces the absorption of the active layer only in the visible region (Zhao et al., 2021).

Figure 10: a) Normalized absorption spectra of pure PBDB-T, Y1, and PTAA films. b) Absorption spectra of PBDB-T/Y1 9:9 (i.e., w/o), PBDB-T/PTAA/Y1 6:1:9 (i.e., w/PTAA), and PBDB-T/Y1 6:9 films

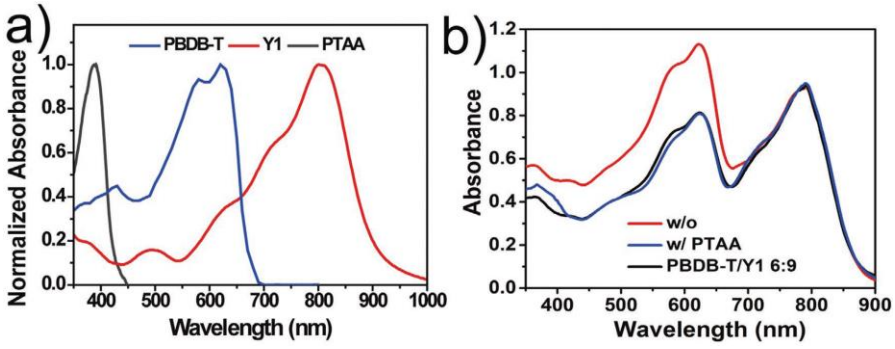

Source: UCLA

The project team achieved a target of approximately 20 percent AVT by using ultrathin Ag (silver) electrodes (Figure 11). The J–V curves and external quantum efficiency (EQE) spectra of opaque OPVs or TOPVs based on PBDB-T/Y1 9:9 (i.e., w/o) or PBDB-T/PTAA/Y1 6:1:9 (i.e., w/ PTAA) under the illumination of an AM 1.5 G solar simulator (100 mW cm^{-2}) are shown in Figure 12. In opaque OPVs (Figure 12a,b), the thickness of an Ag electrode is 100 nm. V_{oc}, J_{sc}, FF, and PCE of PBDB-T/Y1 (9:9) devices are 0.87 V, 22.4 mA cm^{-2}, 69.9 percent, and 13.6 percent, respectively. After the partial substitution of PBDB-T by PTAA (from PBDB-T/Y1 9:9 to PBDB-T/PTAA/Y1 6:1:9), the average J_{sc} decreases from 22.4 to 21.0 mA cm^{-2} due to reduced absorption in the visible region, which finally decreases the average PCE to 13.0 percent. The TOPV devices with an average J_{sc} of 18.2 mA cm^{-2} and an average PCE of 10.6 percent were achieved (AVT = 20.4 percent) with 15 nm Ag electrode. In contrast, because of the reduced absorption in the visible region, a target AVT of approximately 20 percent can be achieved in PBDB-T/PTAA/Y1 6:1:9 devices with a thicker Ag electrode (e.g., 25 nm). The TOPV devices developed by our strategy exhibit higher average J_{sc} of 19.7 mA cm^{-2} (higher EQE value in the IR region, Figure 12d), which leads to a higher average PCE up to 11.7 percent (AVT = 20.1 percent). The champion PCE of PBDB-T/PTAA/ Y1 6:1:9 TOPV device is as high as 12.1 percent, which is one of the best results reported so far. In addition, flexible TOPVs were also demonstrated, a structure of poly(ethylene terephthalate) (PET)/Ag mesh/poly(3,4-ethylenedi-oxythiophene): poly(styrene sulfonate) (PEDOT: PSS) PH1000/ZnO/active layer/MoO_3/ultrathin Au/ultrathin Ag was employed. Comparable device performance (a PCE of 11.7 percent with an AVT of 22.9 percent) was achieved. In conclusion, the "transparent hole transporting frame-works" strategy ensured that ternary blend (PBDB-T/PTAA/Y1) TOPV devices can reach PCEs of 12 percent and AVTs of 20 percent both on rigid and flexible substrates. These results align closely with final project goals of PCEs of 15 percent and AVTs of 30 percent.

Advanced electrodes

Figure 11: Transmittance Curves of Rigid TOPVs

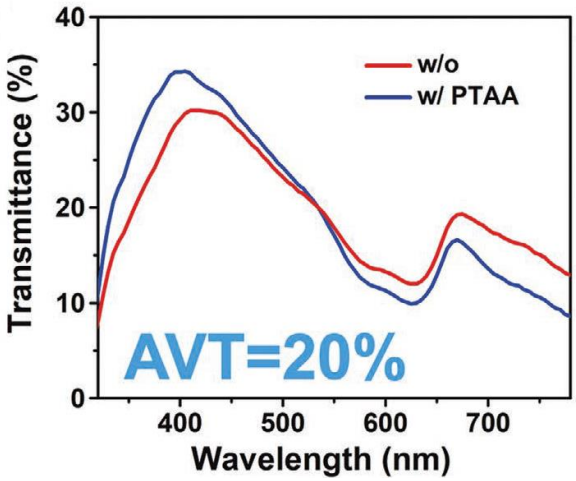

Source: UCLA

Figure 12: a,c) J–V curves and b,d) EQE spectra of opaque OPVs or TOPVs based on PBDB-T/Y1 9:9 (i.e., w/o) or PBDB-T/PTAA/Y1 6:1:9 (i.e., w/ PTAA) under illumination of an AM 1.5G solar simulator, 100 mW cm^{-2}

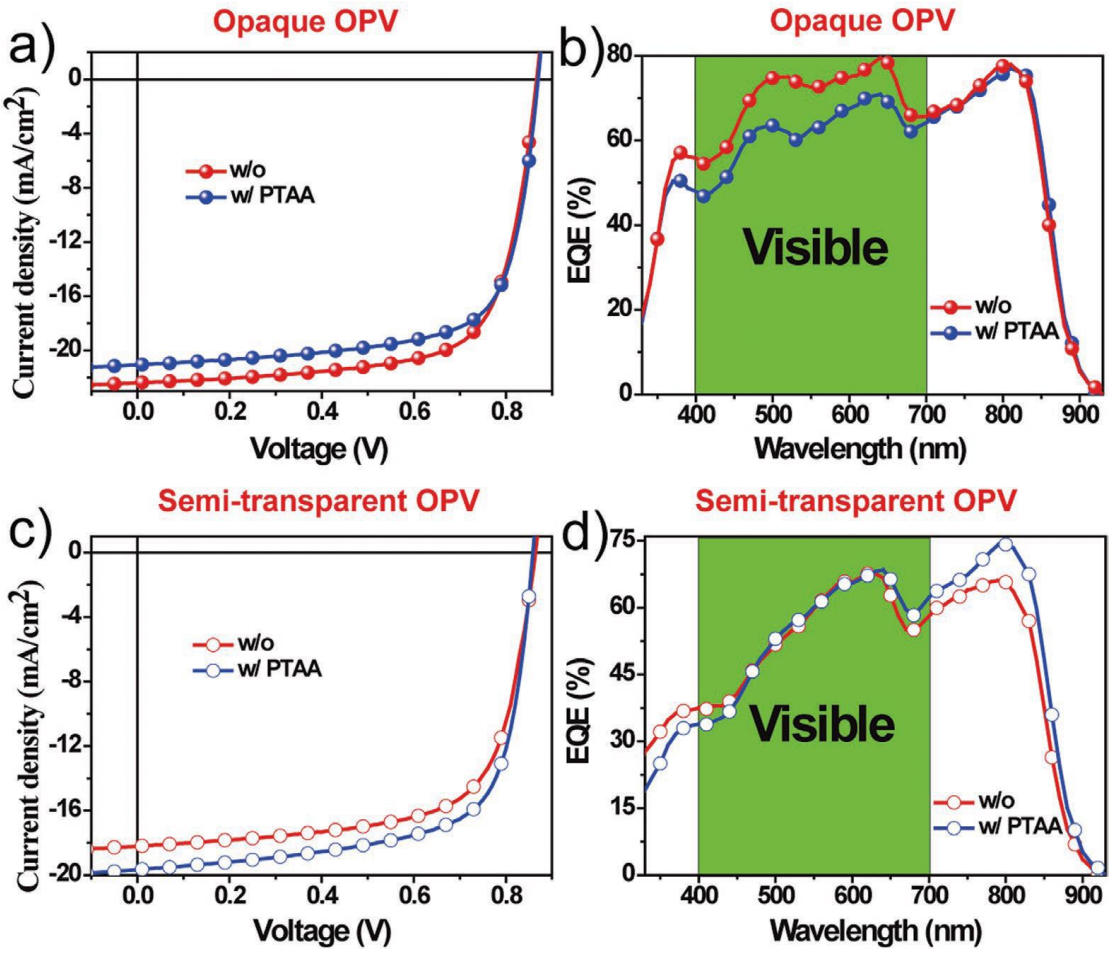

The Ag thickness of opaque OPV (a,b) is 100 nm. The Ag thickness of TOPV (c,d) is 15 nm (for devices without PTAA) and 25 nm (for devices with PTAA), respectively

Source: UCLA

The project team attempted to address the challenge of TOPVs from the perspective of the electrodes with reduced thickness by employing a conducting intermediate layer of poly(3,4-ethylenedioxythiophene) polystyrene sulfonate (PEDOT:PSS) between the hole selective layer (MoO_3 layer for common devices) and the electrodes (ultra-thin Ag layer for common devices) (Zhao et al., 2023). During this stage of the experiment, the project team applied PCE10/POIC as the active layer of the devices. As shown in Figure 13a, there is a clear decrease in overall performance as the devices are made semi-transparent. A huge reduction in J_{sc} exemplifies the issues described above. After applying the PEDOT:PSS modification between the MoO_3 layer and the ultra-thin Ag, we can see a significant enhancement of the device J_{sc}, which aligns closely with the value for opaque devices. From the summary of the device performances in Table 2, the J_{sc} was enhanced by over 15 percent with PEDOT:PSS modification, which resulted in a 13.6 percent PCE enhancement.

Figure 13: a) IV curves of opaque device, TOPVs, and TOPVs with PEDOT:PSS modification. b) Transmittance in the visible region of reference TOPVs, and TOPVs with PEDOT:PSS modification

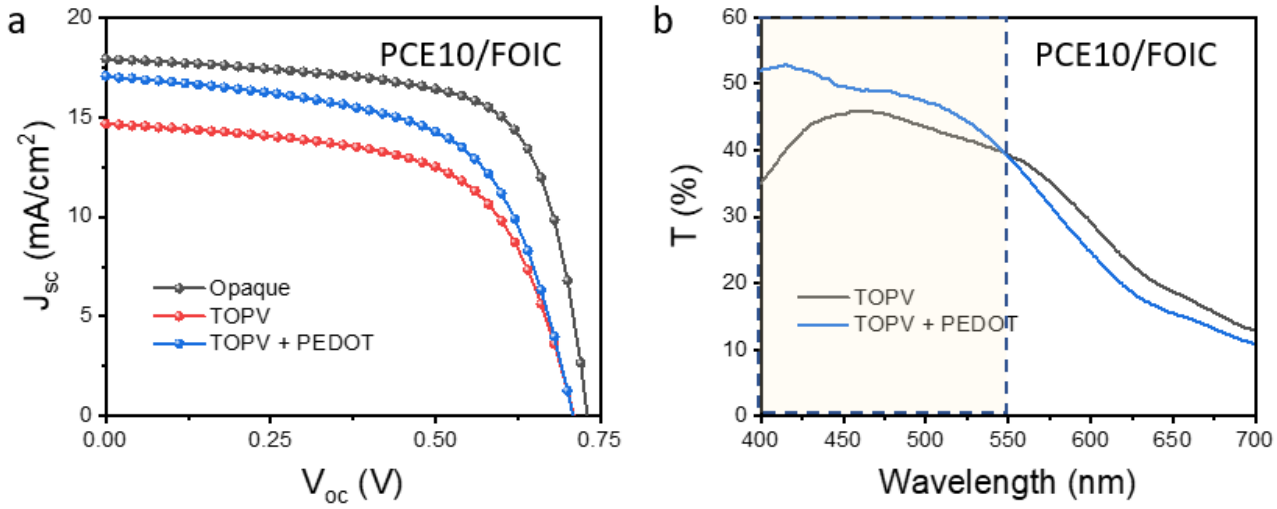

Source: UCLA

Table 2: Summary of photovoltaic performances of opaque device, TOPVs, and TOPVs with PEDOT:PSS modification (PCE10/FOIC as the active layer)

Condition (PCE10/FOIC)	V_{oc} (V)	J_{sc} (mA/cm^2)	FF (%)	PCE (%)
Opaque	0.712	18.13	67.76	8.75
TOPV	0.702	14.75	61.87	6.41
TOPV with PEDOT:PSS	0.708	17.06	60.23	7.28

Moreover, although there is an additional layer of PEDOT:PSS in the device structure, the overall transmittance in the visible region did not decrease. Notably, the AVT of the TOPVs increased from 28.4 percent to 31.5 percent. From the transmittance curves (Figure 13b), the major contribution is shown to be from the better transmittance at the blue wavelength region. This suggests that the PEDOT:PSS modification successfully smoothened the thin MoO_3 layer, which has a discontinuous morphology before modification.

With this promising approach to enhance both the PCE and AVT of the TOPVs devices, the project team further replaced the active layer with one of the highest performing baselines (i.e., PM6/Y6). For the devices with PM6/Y6 as the active layer, a significant enhancement of the short circuit current (J_{sc}) was also obtained after the PEDOT:PSS modification for its conductivity and soft nature (Figure 14).

Figure 14: A) Molecular structure and B) UV-Vis absorption spectrum of the PM6 and Y6 donor and acceptors. C) Schematic employment of intermediate layer of PEDOT:PSS between MoO_3 layer and the ultra-thin Ag layer.

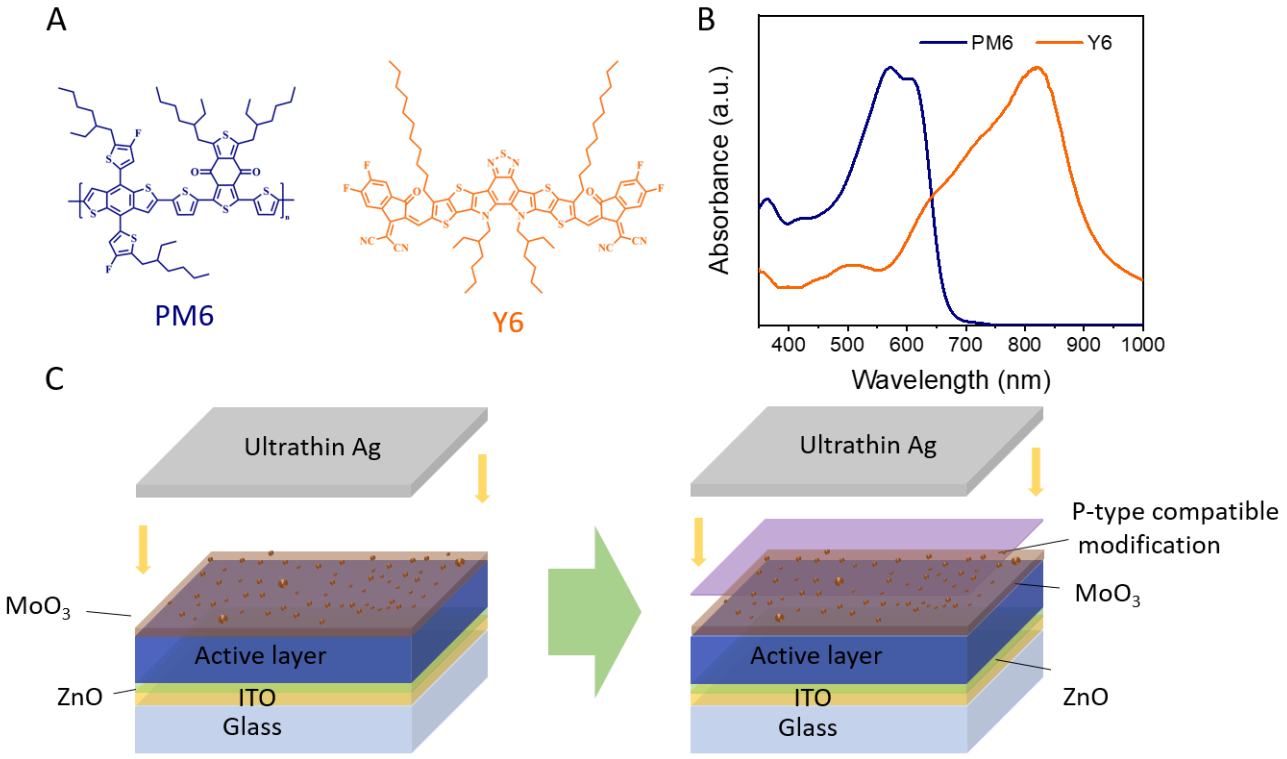

Source: UCLA

The device architecture of opaque OPVs is indium tin oxide (ITO)/zinc oxide (ZnO)/active layer (PM6/Y6)/molybdenum trioxide (MoO_3)/thick silver (Ag) while the device architecture for semitransparent devices is ITO/ZnO/active layer/MoO_3/ultrathin gold (Au)/ultrathin Ag. An ultrathin layer of Au acts as nucleation centers to ensure the formation of a continuous Ag film even at low thickness. As expected, the semitransparent device suffers from a dramatic decrease of current density compared to its opaque counterpart, resulting in a large loss of PCE (Figure 15A). To solve this problem, a dual-functional p-type compatible modification was applied on the MoO_3 layer before the deposition of the ultrathin electrodes (Figure 12C). Notably, from the *I-V* curves of the TOPVs (Figure 15A), the J_{sc} increased from 20.6 mA/cm^2 to 23.7 mA/cm^2 with the application of the PEDOT:PSS modification. Correspondingly, the PCEs of the semitransparent devices were boosted from 12.1 percent to 13.4 percent, which is one of the best results reported so far compared with other studies around the world. (Table 3). The additional p-type soft interlayer did not reduce the AVT of the device (Figure 15B). In fact, the transmittance of the light with wavelengths from 400 nm to 450 nm was strengthened with the modification of dual-functional p-type compatible modification, which resulted in a slight increase of device AVT from 21.1 percent to 22.2 percent. Since both absorption peaks of chlorophyll A and chlorophyll B are in the region of 400 nm to 450 nm, the enhanced transmittance in this wavelength range resulting from the dual-functional p-type compatible modification is quite beneficial to the growth of plants.

Figure 15: a) IV curves of opaque device, TOPVs without and with dual-functional p-type compatible modification. b) Transmittance in the visible region of reference TOPV, and TOPV with dual-functional p-type compatible modification. (PM6/Y6 as the active layer)

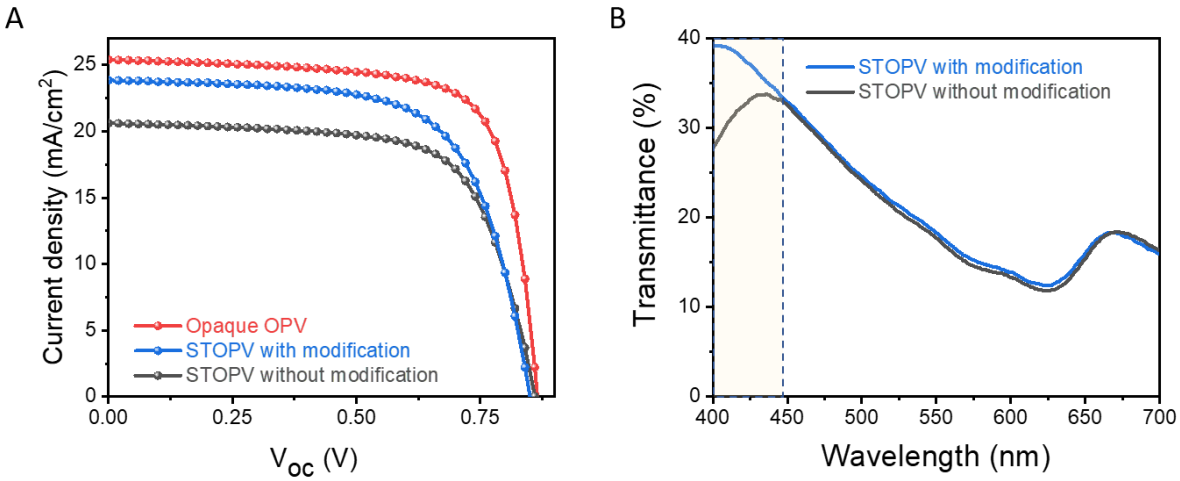

Source: UCLA

Table 3. Summary of photovoltaic performance of opaque device, TOPVs, and TOPVs with dual-functional p-type compatible modification

Devices (PM6/Y6)	V_{oc} (V)	J_{sc} (mA cm-2)	FF (%)	PCE (%)	Average Transmittance from 400 nm to 450 nm (%)
Opaque OPV without the p-type soft interlayer	0.86 ± 0.01	24.3 ± 0.2	73.3 ± 0.3	15.3 ± 0.2 (15.5)	0
STOPV without the p-type soft interlayer	0.85 ± 0.01	20.6 ± 0.3	68.2 ± 0.4	12.1 ± 0.2 (12.3)	32.1 ± 0.6
STOPV with the p-type soft interlayer	0.84 ± 0.01	23.7 ± 0.3	66.5 ± 0.5	13.4 ± 0.3 (13.5)	36.6 ± 0.8

With this promising approach to enhance both the PCE and AVT of the TOPV devices, the project team believes that the enhanced device performance with dual-functional p-type compatible modification originated from 1) enhanced charge carrier extraction, 2) morphology modification of the MoO_3-Ag interface, and 3) adjustment of the optical distribution (Figure 16). Further research will explore and verify these speculations with further characterizations of novel electrodes, including measuring the contact resistance, morphological analysis, and simulating the optical field distribution throughout the devices.

Figure 16: Merits of the PEDOT:PSS modification of the TOPVs devices

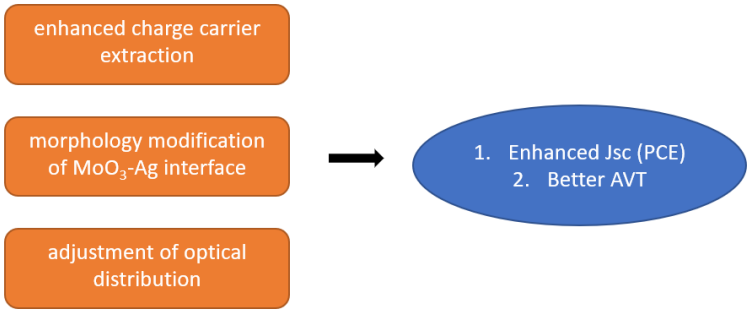

Source: UCLA

With AFM, the project team compared the surface morphology of the PM6/Y6 films coated with MoO_3 layer without and with the p-type soft interlayer (Figure 17). Without the modification, aggregation of MoO_3 on the surface film results in large surface roughness, which can severely undermine the contact between the ultra-thin electrode and the hole selective layer (MoO_3 layer). The root-mean-square roughness was found to be 5.4 nm. In contrast, the film with the p-type soft interlayer showed significantly reduced root-mean-square surface roughness of 2.1 nm, which is beneficial to the deposition of the metal electrodes. The team was able to more directly observe the variation of the MoO_3 layer surfaces when plotting the height profile from the AFM images along the dashed middle line. The surface without the p-type soft interlayer showed much larger height variation than the one with the interlayer, which also indicates much better contact can be expected with interface amelioration by the p-type soft layer.

Figure 17: (A) Transmittance curves of TOPVs based on PM6/Y6 with and without the p-type interlayer. (B) Height vibration of across the dash line on (C) AFM image of the MoO_3 surface without the p-type soft interlayer and (D) AFM image of the MoO_3 surface with the p-type soft interlayer.

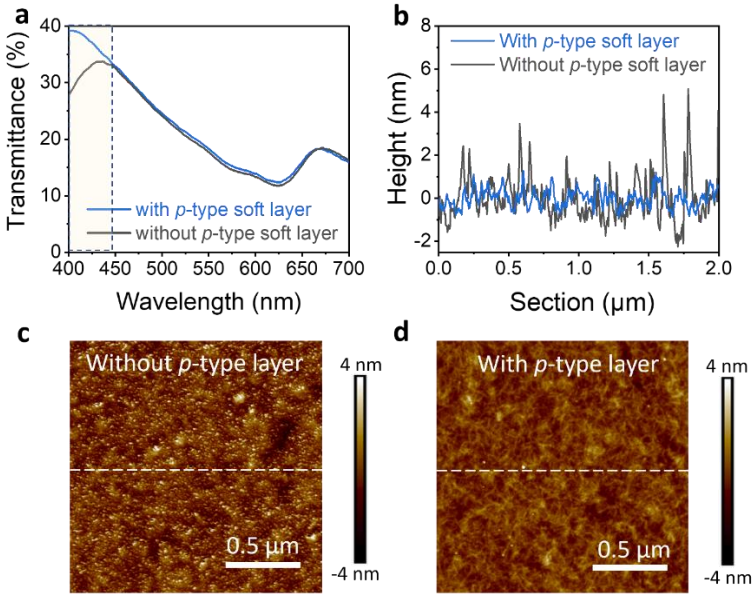

Source: UCLA

To investigate the contact resistance of the devices, the project team applied the transmission line method on the MoO_3-coated active layer with and without the p-type soft interlayer. For the electrodes, a layer of Au with 1 nm thickness was deposited first and then a layer of Ag with 100 nm thickness was added. The total resistance, R_T, between two contacts was measured and plotted as a function of contact spacing, "d", as shown in Figure 18A. The total resistance is approximately the sum of the contact resistances at the interfaces and the sheet resistance through the film. As contact spacing "d" increases, the sheet resistance of the underlying film should increase proportionally, thus sheet resistance can be isolated by linearly fitting the plot of R_T vs d. Therefore, by extrapolating the fitted data, the project team obtained the contact resistance (R_C) as R_T at d = 0. A large decrease of R_C from 22.74 kΩmm to 9.49 kΩmm was measured after the modification of the p-type interlayer, which also indicates much better carrier extraction efficiency and less recombination in the modified devices. Electrochemical impedance spectroscopy (EIS) measurements were also performed, to further observe the contact effects. For this measurement, the cell was biased to its open-circuit potential, then probed with a low amplitude AC voltage signal. The current was measured for a range of AC frequencies to observe the change of device impedance. The project team fitted Nyquist plots of the devices (Figure 18B) with the equivalent circuit (inset of Figure 18B), where the impedance response of the solar cell at low frequencies is related to the recombination resistance (R_{rec}), and at high frequencies to the charge transfer resistance (R_t). R_{rec} represents the recombination processes in the bulk, while R_t is the series resistance in the device and is associated with the charge extraction at the electrodes. The R_{rec} of the devices with and without the p-type soft interlayer were similar (the R_{rec} without the p-type interlayer was 6.2 Ω, while the R_{rec} with the p-type soft interlayer was 5.2 Ω). But the R_t of the devices differ greatly. After the modification, the R_t reduced from 257.7 Ω to 67.3 Ω, illustrating an enhanced extraction of the charge carriers. To analyze the charge extraction properties, the project team measured the photocurrent density (J_{ph}) versus the effective voltage (V_{eff}) of the TOPVs with and without the p-type soft interlayer (Figure 18C). The value of J_{ph} is defined as $J_L - J_D$, where J_L and J_D are the current densities under illumination and in dark conditions, respectively. The term V_{eff} is defined by $V_0 - V$, where V_0 is the voltage when $J_{ph} = 0$ and V is the applied voltage. At high V_{eff}, all the photogenerated excitons are dissociated into free charge carriers and collected by electrodes, and the saturation photocurrent density (J_{sat}) is only limited by the absorbed incident photons. The project team obtained a higher J_{ph}/J_{sat} of PEDOT:PSS modified device at low electric field than that of the device without the p-type interlayer, which the team attributed to the enhanced charge extraction efficiency. The team also measured transient photocurrent (TPC) of the devices to further investigate the charge carrier extraction of the solar cells with and without the p-type soft interlayer. The TPC curves exhibited a significantly faster decay for devices with the p-type soft interlayer (Figure 18D), which means a notable enhancement of charge extraction rate. Better charge extraction with less carrier recombination explains the higher J_{sc} obtained from the J-V tests.

Figure 18: (A) Contact resistance measurements of TOPVs based on PM6/Y6 with and without the p-type interlayer by transmission line method. (B) EIS data of TOPVs based on PM6/Y6 with and without the p-type soft interlayer. (C) Corrected photocurrent data as a function of the potential difference V_0–V. (D) TPC for TOPVs based on PM6/Y6 with and without the p-type soft interlayer.

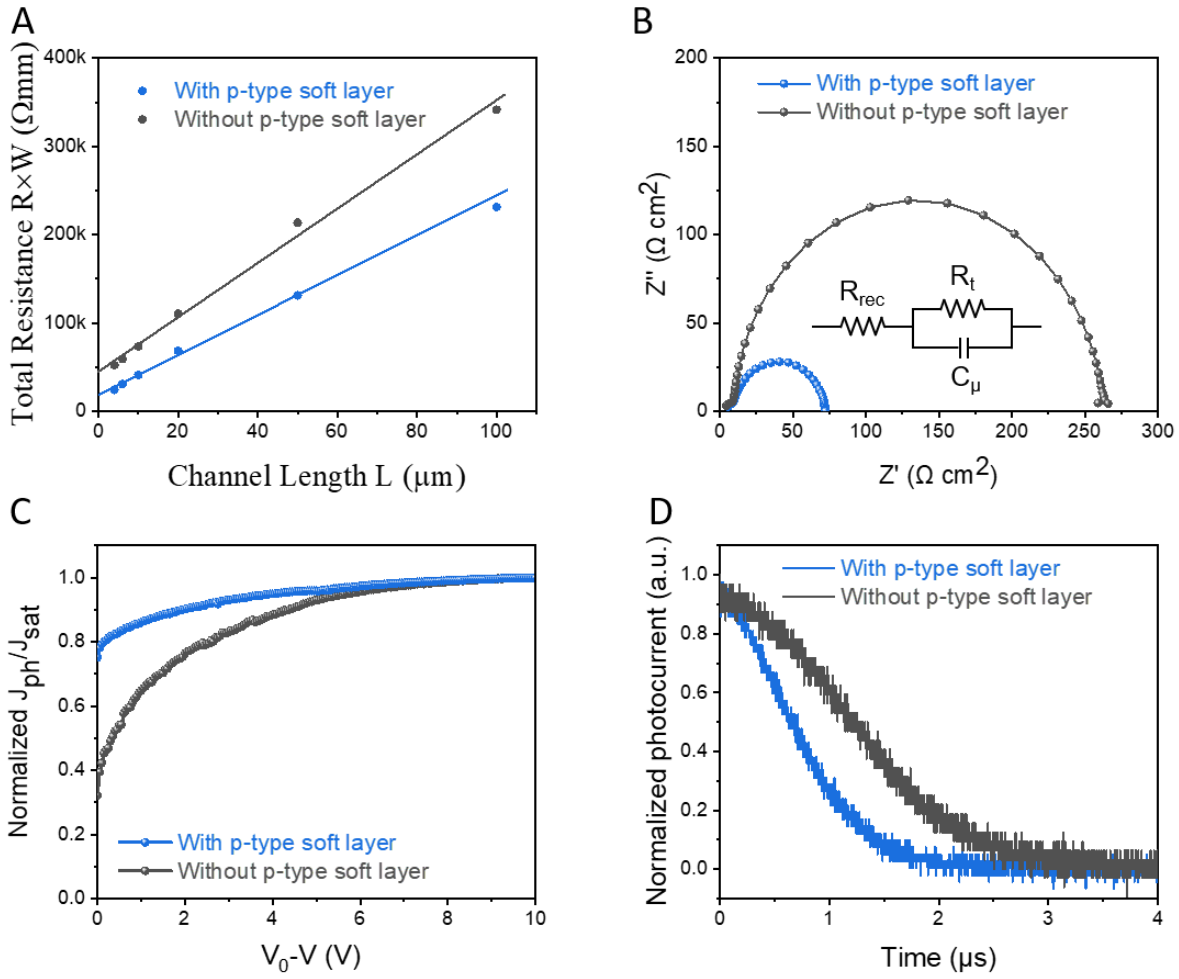

Source: UCLA

In summary, to counter the reduction of TOPV efficiency when using thinner electrodes, the project team utilized a p-type interlayer to modify the interface between hole selective layer and the electrodes of the semitransparent devices. With this strategy, the charge carrier extraction of the devices was successfully improved by contact optimization at the interface of the hole selective layer and the electrode and the reduction of the contact resistance. AVT and the photon absorption by the active layer were simultaneously enhanced. As a result, the J_{sc} of the TOPVs with PM6/Y6 as active layer increased from 20.6 mA/cm^2 to 23.8 mA/cm^2, which led to an averaged PCE of 13.4 percent. Furthermore, a AVT of 22.2 percent was achieved after applying the p-type interlayer. The p-type interlayer is beneficial to both the energy conversion efficiency of the TOPVs and the transmittance of visible light through the devices. This work highlights the importance of considering the issue of impaired charge transportation with thinned device electrodes and provides important insights into using interface

modification to develop semitransparent devices with high PCE and favorable AVT for commercial applications.

Advanced Interface Layers

To improve the interface property of OPVs, the project team developed a powerful reductive interlayer based on L-glutathione reduced (L-G, Figure 19a and 19b) with PM6/Y6 as the active layer. With the insertion of the interlayer, the PCE of the semitransparent devices increased from 11.6 percent to 13.5 percent, with an enhancement of J_{SC} from 20.5 to 22.2 mA/cm^2. This led to a lower interface resistance and facilitating charge transfer between the ZnO layer and the PM6/Y6 active layer. Additionally, due to the strong reducibility of the L-G molecule, the production of the superoxide radicals was significantly reduced. Density functional theory (DFT) quantum mechanical simulation calculations with PBE-D3 confirmed the defect passivation effect from the functional groups of the L-G molecules as well as the superoxide radical suppression effect. After continuous illumination with 1-sun intensity for 300 hours, the molecular structure and packing in the organic active layer remain almost unchanged, while the reference active layer showed a distinct decomposition. The TOPVs with the L-G interlayer maintained over 84 percent of their initial PCE after 1008-hour continuous illumination. The integration of the resulting TOPV in a power-generating roof demonstrated that plant growth in the TOPV-integrated greenhouse is comparable to that of a traditional glass-roof greenhouse. These results reinforced the feasibility of the TOPVs in agricultural applications and other practical scenarios. As shown in Figure 19b, the basic device architecture for our TOPVs is ITO/ZnO/active layer/MoO_3/ultrathin Au/ultrathin Ag. The ultrathin layer of Au provides nucleation centers to ensure the formation of a continuous Ag film even with small thickness. A thin L-G interlayer was inserted between the ZnO layer and the active layer via spin-coating and annealing processes. As confirmed by atomic force microscope images, the morphologies of the ZnO film surface did not significantly change with the incorporation of the L-G layer. The J-V curves of the devices with the interlayer show a significant enhancement of the J_{SC} (increase from 20.5 mA/cm^2 to 22.2 mA/cm^2, Figure 19c). As a result, the averaged PCE of the semitransparent devices increased from 11.6 percent to 13.5 percent (other parameters are summarized in Table 4). The EQE spectra confirmed the enhanced J_{SC} upon the incorporation of the L-G interlayer (Figure 19d). The transmittance measurements showed similar AVTs of the devices with and without the L-G interlayer, which indicated that the insertion of the interlayer did not influence the transparency of the semitransparent solar cells (Figure 19e). To evaluate the bifacial properties of the semitransparent devices, the project team also measured the reflectance and J-V curves of the devices with the interlayer from the Ag side. A PCE of 3.6 percent with reflectance of 49.1 percent from 400 nm to 700 nm was obtained.

Table 4: Photoelectric performances and the stability under continuous 1-sun illumination of TOPVs based on PM6/Y6 with and without the L-G interlayer.

Condition (PM6/Y6)	Voc (V)	J_{sc} (mA/cm²)	FF (%)	PCE (%)	AVT (%)	PCE retaining after 1008 hours (%)
TOPV without L-G interlayer	0.84 ± 0.01	20.5 ± 0.2	67.2 ± 0.3	11.6 ± 0.4	21.2 ± 0.3	18.4 ± 6.0
TOPV with L-G interlayer	0.86 ± 0.01	22.2 ± 0.3	70.4 ± 0.4	13.5 ± 0.4	21.5 ± 0.3	84.8 ± 3.7

Figure 19: (a) Molecular structures of L-glutathione reduced. (b) Device architecture of TOPVs with L-G interlayer. (c) *J–V* curves, (d) EQE spectra, and (e) transmittance measurements of the devices with and without the L-G interlayer. (f) Nyquist plots (inset: the equivalent circuit), (g) TPC curves, and (h) photocurrent data as a function of the potential difference V_0–V of the devices with and without the L-G interlayer.

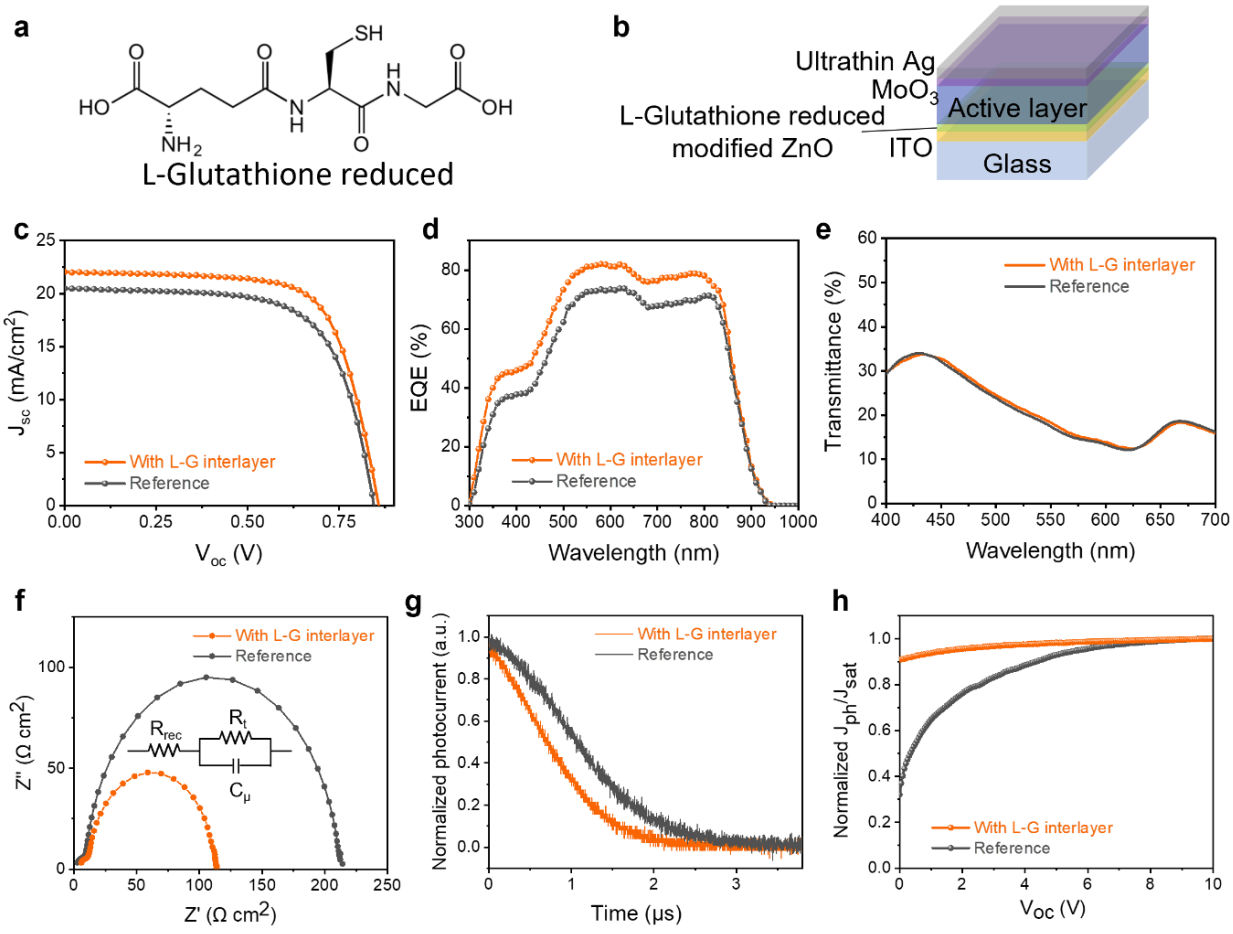

Source: UCLA

The project team compared the contact resistance of the devices EIS measurements. The cells were biased to their open-circuit potential and probed with a low amplitude AC voltage signal. The current was measured for a range of AC frequencies to observe the change of device impedance. The team fitted the Nyquist plots of the devices (Figure 19f) with the equivalent circuit (inset of Figure 19f). The impedance response of the semitransparent solar cells at low frequencies is related to R_{rec}, and the impedance response at high frequencies is related to R_t. The results showed that the R_{rec} values of the semitransparent devices with and without the L-G interlayer were similar (the R_{rec} without the L-G interlayer was 10.1 Ω cm^2, while the R_{rec} with the L-G soft interlayer was 10.8 Ω cm^2). In contrast, the R_t reduced from 203.4 Ω cm^2 to 102.5 Ω cm^2 after the incorporation of the L-G interlayer. This result proves that a much lower charge transfer resistance was obtained by the insertion of the L-G interlayer. The team also measured TPC of TOPVs to further analyze the charge carrier extraction of the solar cells with and without the L-G interlayer. The TPC curves exhibited a significantly faster decay for devices with the interlayer (Figure 19g), indicating a notable enhancement of charge extraction rate. Better charge extraction with less carrier recombination explains the higher J_{sc} obtained from the J-V tests. The atomic force microscopy AFM images of the ZnO surface with and without the L-G interlayer did not exhibit an obvious difference in the morphology. The ZnO surface with L-G interlayer has slightly lower roughness (from 4.6 nm to 3.3 nm), which should contribute to facilitated charge transport. To further investigate the charge extraction properties of the TOPVs with and without the L-G interlayer, we measured J_{ph} versus V_{eff} of the devices (Figure 19h). The value of J_{ph} is defined as J_L - J_D, where J_L and J_D are the current densities under illumination and in dark conditions, respectively. V_{eff} is defined by V_0 - V, where V_0 is the voltage when J_{ph} = 0 and V is the applied voltage. At high V_{eff}, all the photogenerated excitons are dissociated into free charge carriers and collected by electrodes, and J_{sat} is only limited by the absorbed incident photons. The project team obtained a higher J_{ph}/J_{sat} of the semitransparent device with the L-G interlayer at low electric field than that without the interlayer. It suggests facilitated charge transfer at the interface between the electron transport layer and the active layer, leading to an enhanced charge extraction efficiency with the L-G interlayer.

To understand the physical mechanism underlying the defect passivation effect of the L-G interlayer, the project team carried out DFT calculations. The team first calculated the defect formation energy (DFE) of the wurtzite ZnO surface and identified the two major defects that are easy to form in the ZnO film (i.e., oxygen vacancy (DFE: 0.27 eV) and zinc interstitial (DFE: 1.05 eV)) (Figure 20a and 20b). The L-G molecule mainly consists of three parts: glutamate, cysteine, and glycine (Figure 20c). The project team separately simulated the interaction energy of each part with the two defects. The cysteine turns out to have a strong interaction with the oxygen vacancy (Inter. Ener.: -4.98 eV) while the glycine interacts tightly with the zinc interstitial (Inter. Ener.: -5.46 eV) (Figure 20d-i). This indicates that the L-G molecule can effectively nullify both major defects in the ZnO film, thus reducing the contact resistance and facilitating the charge transport through the device. The passivation effect of the L-G interlayer can also be confirmed by the enhanced internal quantum efficiency (IQE) of the semitransparent device with the L-G interlayer compared to the IQE of the opaque device without the L-G interlayer. Further, we investigated the influence of L-G on the superoxide formation. There is almost no interaction between the oxygen molecule and the perfect ZnO

surface. However, the oxygen vacancy on the ZnO surface can interact with the oxygen molecule and charge transfer occurs from the surface to the oxygen molecule, which is a necessity for superoxide formation. In the presence of the L-G molecule, oxygen is not attracted by the oxygen vacancy since the defect is already nullified by the cysteine part of the L-G. The charge transfer from the ZnO surface to the O_2 is impeded by the L-G molecule, avoiding the formation of the superoxide molecule. Thus, from these simulation results, two different functions of the L-G interlayer can be elaborated. The first effect of the L-G interlayer on the ZnO layer is defect passivation. The strong interactions between the L-G molecule and the charge defects on the ZnO surface (i.e., oxygen vacancy and zinc interstitial) can alleviate the charge carrier trapping ability of the defects. The second effect is that the reductive L-G molecule can effectively suppress the superoxide formation, which is usually triggered by the oxygen vacancy on the ZnO surface.

Figure 20: (a) Oxygen vacancy and (b) zinc interstitial defects on the ZnO surface. (c) Three parts of L-Glutathione: glutamate, cysteine, and glycine. Interaction energies of oxygen vacancy and zinc interstitial defects with (d) glutamate, (e) cysteine, and (f) glycine part of L-Glutathione.

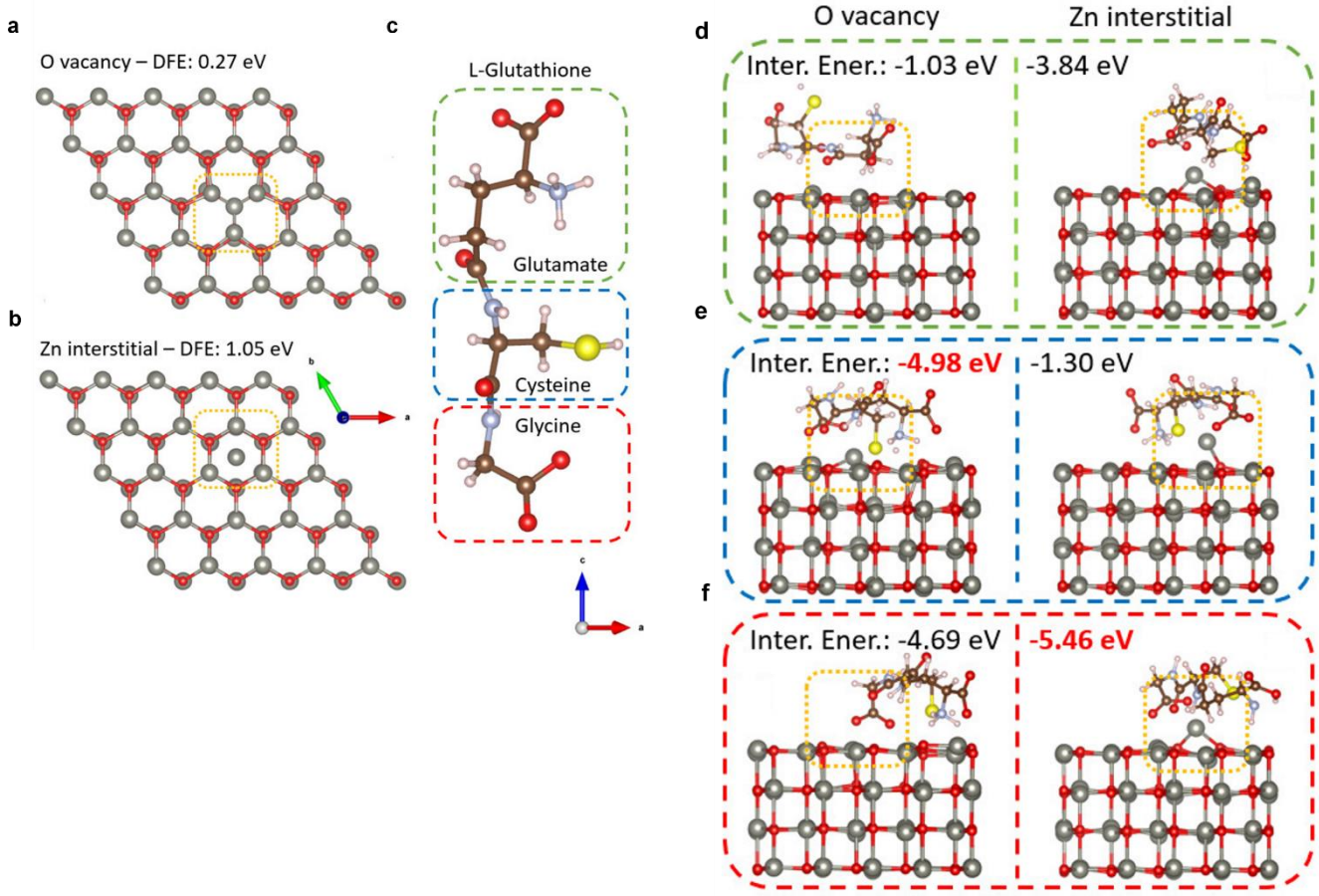

Source: UCLA

To assess the active layer changes under continuous solar radiation, the project team compared the grazing-incidence wide-angle X-ray scattering (GIWAXS) patterns of the PM6/Y6 films on ZnO films with and without the L-G interlayer. As shown in Figure 21a, the 2D

GIWAXS patterns are similar prior to continuous radiation. The diffraction peak at q = 1.73 $Å^{-1}$ along the profiles in out-of-plane (OOP) direction was assigned to be the π-π stacking of the PM6, while the diffraction peak at q = 0.29 $Å^{-1}$ along the in-plane (IP) direction was assigned to be the lamellar stacking of either Y6 or PM6. Upon 500-hour continuous radiation under 1-sun intensity in ambient air, along the OOP direction the π-π stacking peak of the film on the ZnO layer with and without the L-G interlayer did not change (Figure 21b). In contrast, the distinct peak broadening of π-π stacking of the film directly onto the ZnO layer indicated organic molecular destruction and the morphology change of the active layer after the continuous radiation. The 1-D profile of the film on the ZnO layer without the L-G interlayer along the IP direction also showed a broadened peak at q = 0.29 $Å^{-1}$ after the continuous radiation, suggesting the break-down of the lamellar structure (Figure 21c). An additional peak at q = 0.43 $Å^{-1}$ showed up at the IP direction of the reference sample after the continuous radiation in air, which did not appear in the sample with the L-G interlayer. This peak should be attributed to the lamellar packing of the Y6 molecules. This indicated that the phase separation was suppressed by the interaction between the active layer and the L-G interlayer. The GIWAXS patterns proved that the incorporation of the L-G interlayer can both suppress the degradation of the active layer and remit its molecular aggregation during the stability tests.

Figure 21: (a) 2D GIWAXS patterns of the PM6/Y6 films on ZnO films with and without the L-G interlayer before and after illumination under 1-sun intensity for 500 hours, and corresponding 1D GIWAXS profiles in (b) out-of-plane and (c) in-plane direction (incident angle: 0.13°).

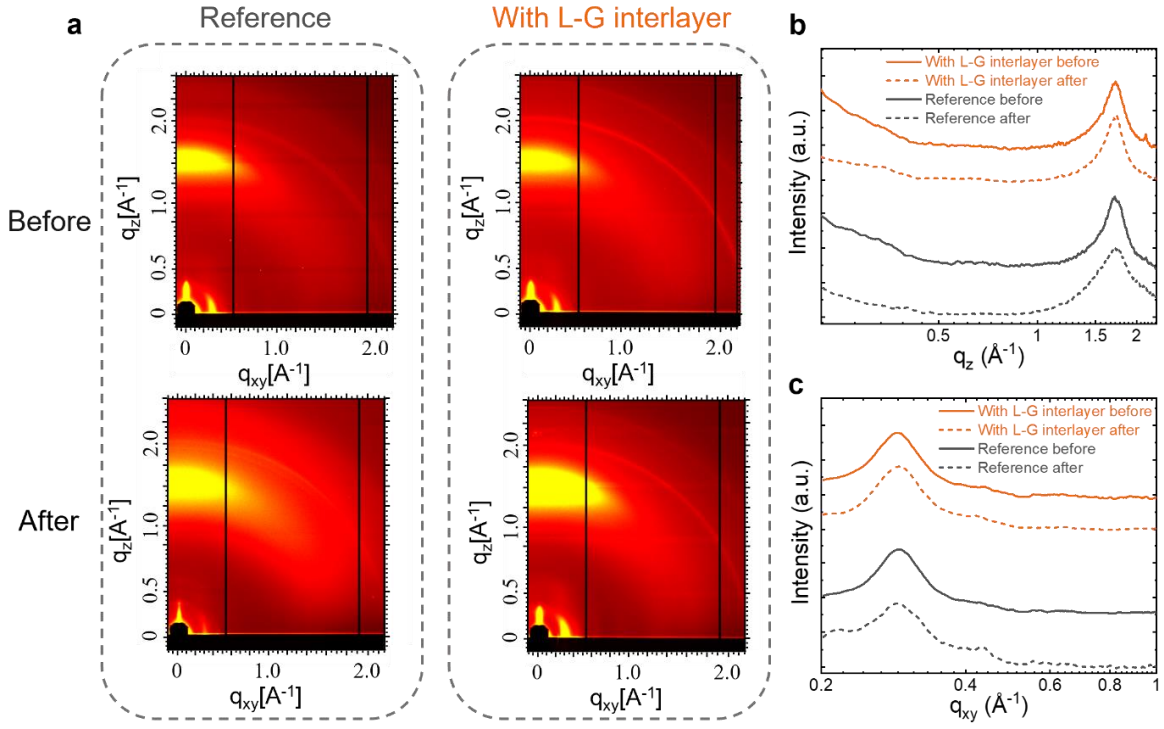

Source: UCLA

The project team then compared the C 1s XPS spectra of the active layer films with and without the L-G interlayer before and after 300-hour continuous radiation (Figure 22a). The

reference film without the interlayer showed a distinct C-O shoulder peak after the exposure, while the spectra of the film with the interlayer remained roughly the same. This proved that the reductive interlayer successfully impeded the oxidation of the organic molecules in the active layer. The EPR spectra showed that with the L-G interlayer the superoxide radical signal was greatly reduced under UV radiation. In comparison, the films without UV radiation did not show a distinguishable signal. This result manifested the suppression of the superoxide of the L-G molecule, which agreed with the simulation data. To detect the superoxide level inside of the active layer, the team further used hydroethidine as the radical trap (HE probe), which can easily react with the superoxide radicals and transform into ethidium with different photoluminescence peak positions (Figure 22b). The superoxide generation rate in the organic active layer with the interlayer is distinctly slower, once again confirming the superoxide suppression effect. The project team used coumarin (a compound that specifically reacts with hydroxide radicals and produces strong luminescence) to investigate the generation rate of the hydroxide radicals of the ZnO films with and without the L-G interlayer. The results show that the hydroxide radicals are also largely suppressed by the L-G interlayer.

The suppressed superoxide and hydroxide radical generation notably led to enhanced operational stability of the encapsulated TOPV devices based on PM6/Y6 (Figure 22c). The devices with the L-G interlayer maintained over 84 percent of their initial efficiency after exposure of 1,008-hours under continuous illumination with a metal-halogen xenon lamp source (90 ± 10 mW cm^{-2}) at a temperature around 45 °C and relative humidity about 40 percent (Figure 22d). The team further tested the thermal stability of the TOPV devices with and without the L-G interlayer in an inert environment. The devices with the interlayer maintained over 70 percent of their initial PCEs while the references lost about 95 percent of the initial PCEs. This can be attributed to the interactions between the L-G interlayer and the active layer molecules. The interactions alleviated the molecule aggregation and phase separation of the active layer during the stability tests. This result is also confirmed by the morphology changes of the active layers on ZnO layer with and without the L-G interlayer.

Figure 22: (a) C 1s XPS spectra of the active layer films with and without the L-G interlayer before and after 300-hour continuous radiation. (b) Reaction that the hydroethidine transforms into ethidium the superoxide radicals. (c) Normalized fluorescence intensity of the HE probe as a function of illumination time under AM1.5G illumination conditions. $I_F(t)$ is the fluorescence maximum at time t and $I_F(t_0)$ is the background fluorescence intensity. $I_F(t)/I_F(t_0)$ corresponds to the yield of superoxide generation. (d) PCE changes of the devices with and without L-G interlayer during 1008-hour exposure under continuous illumination.

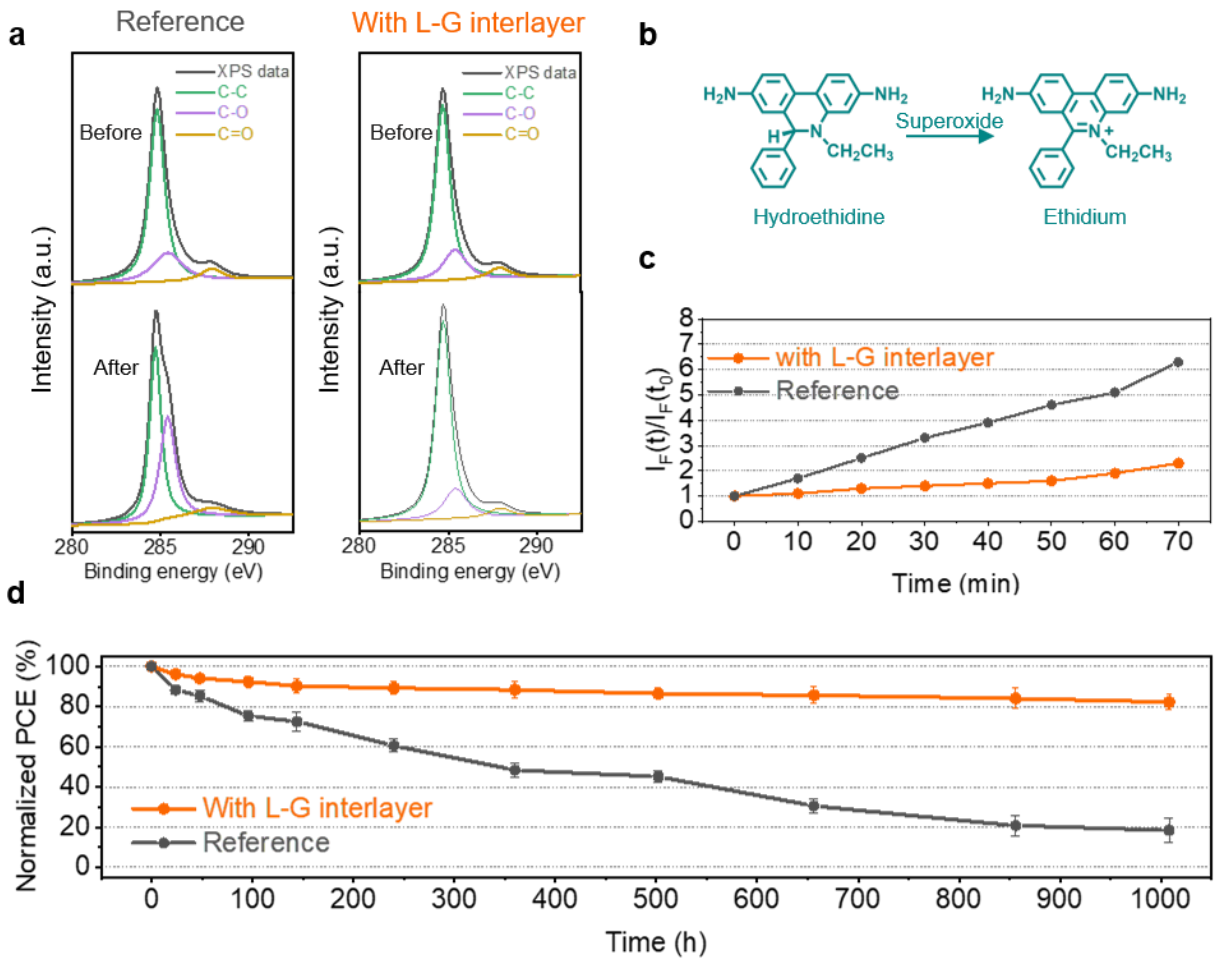

Source: UCLA

Aiming to resolve the stability issue of the TOPVs for an agricultural application, the project team introduced a reductive interlayer into the device architecture. The charge carrier extraction and transportation were enhanced due to the nullification of the charged charger traps in the ZnO layer. The insertion of the L-G interlayer led to an improved average PCE of 13.5 percent while maintaining the AVT of the semitransparent devices. The suppression of the superoxide generation was observed under the radiation. As a result, the devices with the interlayer maintained a PCE over 84 percent after continuous illumination for 1,008 hours.

New Structures of TOPV Devices

The project team verified the reproducibility of the new device structure for TOPVs with an extra anti-reflection coating (ARC). The ARC was made by coating ZnO (zinc oxide) nanoparticles under the original glass substrate (Figure 23a). The project team confirmed that the ARC layer enhanced both AVT and PCE for the TOPV devices (Figure 23b,c). To confirm reproducibility, the team made over 20 devices and summarized their performances. The resulting statistical data showed that the ARC layer effectively improved the AVT of devices by 1 percent and the PCE by 0.3 percent (Figure 23d,e).

Figure 23: (a) Scheme of the new device structure with ARC. (b) Transmittance spectra and (c) corresponding *J-V* curves of semitransparent devices with and without the ARC layer. The statistical data of (d) PCEs and (e) AVTs of semitransparent devices with and without the ARC layer.

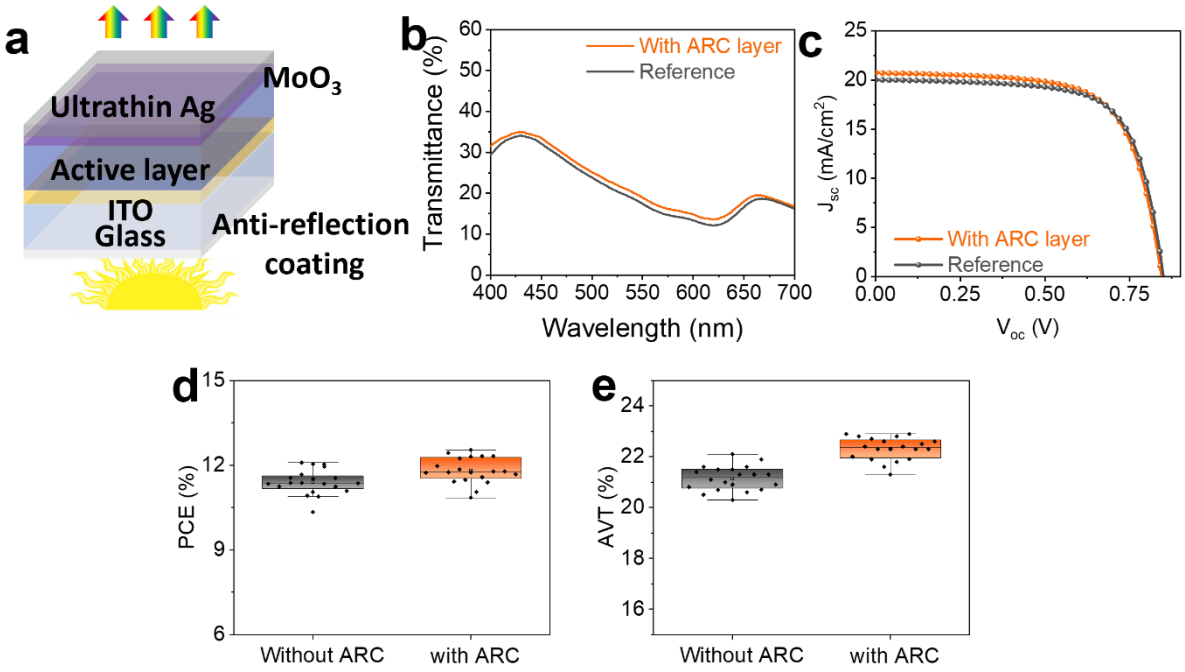

Source: UCLA

TOPVs on the roof and/or windows of a miniaturized lab-scale "smart greenhouse" to harvest solar energy, while enabling photosynthesis needed for plant growth

To verify the capability of growing various plants in the smart greenhouse system, the project team built model scale greenhouses with the OPV devices with the L-G interlayer as the greenhouse roofs and compared the growth of multiple common crops (i.e., mung bean, wheat, and broccoli sprout) under these roofs with those grown in greenhouses with roofs of normal transparent glass or segmented inorganic solar cells (Figure 24a). The project team monitored the growing conditions of the plants for eight consecutive days under natural sunlight without a UV filter. As summarized in Figures 24b to 24d, the team measured sprout lengths, length deviations, biomass productivities, and survival rates of the plants after the

eight-day growth period. Since the wheat sprouts do not have leaves, the team only included the leaf area data for the mung bean and broccoli samples. The sprout lengths and survival ratios of the plants grown in the greenhouses with TOPV roofs were higher than those grown in the greenhouses with transparent glass roofs or spatially segmented inorganic solar cell roofs. This result can be attributed to the UV-light absorbing properties of the roofs that are fully covered with TOPVs as the UV exposure undermines the biological activity of the sprouts. To confirm this, the project team also integrated a UV filter over the greenhouses during another batch of plant growth. The height, number of branches, and the leaf area of the sprouts that grew under the transparent glass roof were comparable, or slightly higher than, those grown in the greenhouse with the TOPV roof. This suggests that the integration of TOPVs as a greenhouse roof will not impair the growth of plants, and in fact will protect plants from detrimental UV exposure. The biomass productivity together with the concurrent electricity production of the system was also estimated as indicated in Figure 24b-d. Combined with the elongated operational lifetime of the TOPVs with the L-G interlayer, successful commercialization of environmentally friendly greenhouses is expected.

Figure 24: (a) Scheme of the power-generating greenhouse with TOPV roof, and plant growth conditions of (b) mung bean, (c) wheat, and (d) broccoli. Biomass among the different plants was normalized into the final mass with 1 gram initial seed mass. Survival count was normalized into the number of survived plants per 100 initial seeds.

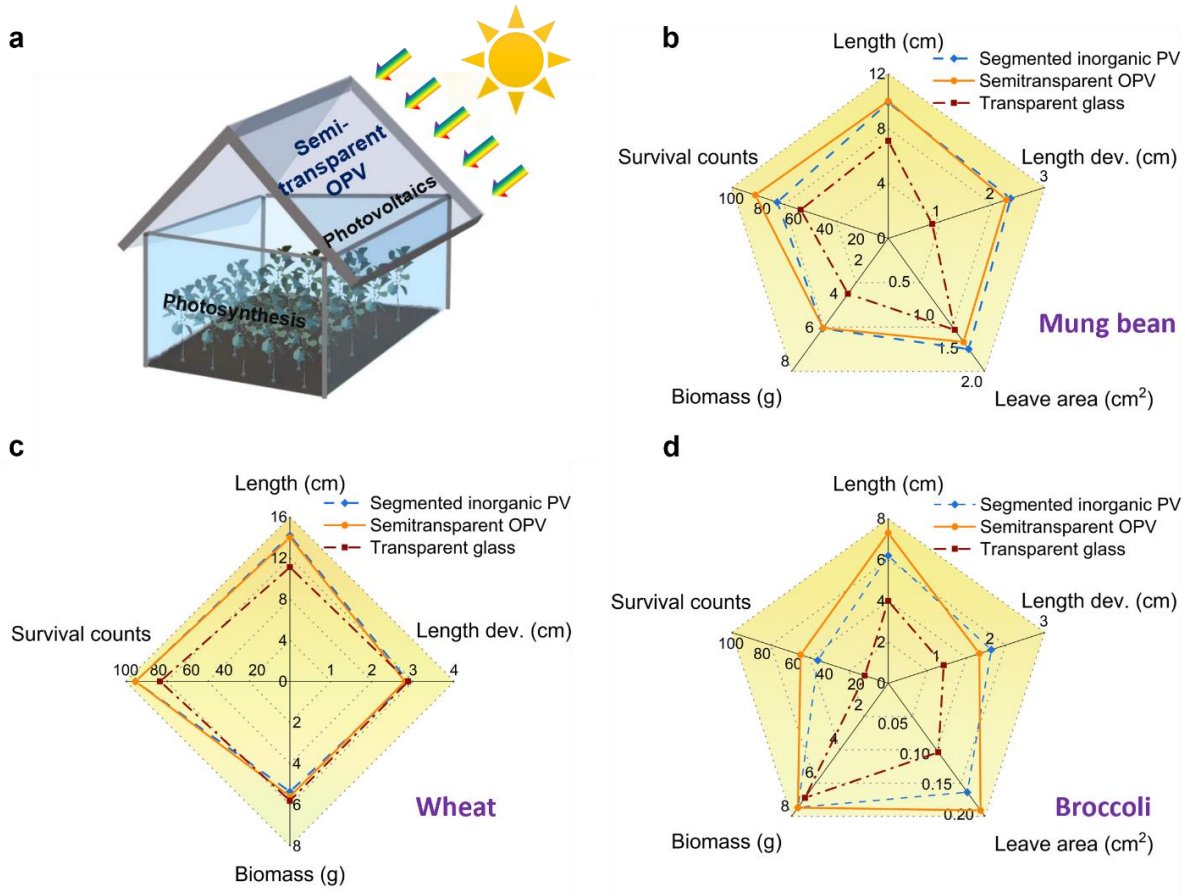

Source: UCLA

Technical Barriers and Challenges

During the project, the team encountered several technical challenges. Delays as a result of the COVID-19 pandemic affected technical milestones, which the project team was able to overcome. At the initial stage, the team lacked experience to make large-size solar panels over 0.1 cm^2 and did not have a large coating machine for device fabrication. The project team learned from colleagues in academia and industry and quickly overcame these problems. The team struggled with the size of the vacuum chamber for the electrode coating of the large-scale solar PV panels for the smart greenhouse. The equipment costs over $50,000, which was beyond the financial support currently available for the project.

Project Activities

The project team published a paper in the prestigious journal, *Nature Sustainability* 1-10 (2023), which was widely reported by multiple media outlets such as Optics & Photonics News, EurekAlert!, Tech Xplore, Scinexx, Gizmag Emerging Technology Magazine, and Interesting Engineering. Articles in the journal *Advanced Materials* were reported by Nanoer and Top Chemistry Research. Several company holders and research centers have contacted the team regarding the OPV technology. AcclimateUs asked the team about the greenhouse experiment. The University of California Agricultural and Natural Resources South Coast Research and Extension Center contacted the team regarding the semitransparent OPV roof.

CHAPTER 4: Conclusion

Sustainable technologies that efficiently utilize farmland are a key approach to addressing global food and energy challenges. Greenhouses, in particular, can effectively prolong the cultivation season by remitting fluctuating weather and/or temperature influences over crops and may be an effective strategy to boost food yield for a growing human population. However, controlling conditions in greenhouse environments consumes a considerable amount of power; thus, a smart greenhouse with semitransparent photovoltaics integrated into a power-generating roof may be a desirable solution for modern agriculture (Liu et al., 2021) (Meng et al., 2021). In accomplishing both efficient plant photosynthesis and electrification from sunlight, this project designed five approaches to reach the final goal of 15 percent PCE and 30 percent AVT for organic solar cells. First, new IR absorbing donor and acceptor materials via side chain engineering were synthesized. Adopted alkoxyl groups red-shifted the absorption range to the IR region while retaining the same or better solubility for the material processing. The device developed in the first stage led the project team closer to the final goal by achieving 13 percent PCE, 21 mA cm−2 J_{sc}, 0.87 V V_{oc}, and 69.9 percent FF. Second, the team employed a PEDOT:PSS interlayer to counter the reduction of the PCE. The charge carrier extraction of the devices was successfully improved by contact optimization at the interface. This led to an average PCE of 13.4 percent with AVT of 22.2 percent. Third, a reductive L-G interlayer was introduced into the device architecture to resolve the photostability issue for the TOPV devices. This nullified the charged charge traps in the ZnO layer such that the charge carrier extraction and transportation were enhanced. The device showed an average PCE of 13.5 percent with AVT of 22.2 percent while maintaining performance over 84 percent with continuous illumination for 1,008 hours. Fourth, the team verified the new structure of TOPV devices with an anti-reflection layer. The coated ZnO nanoparticles for reflection enhanced both averaged PCE and AVT by 0.3 percent and 1 percent, respectively. Finally, a miniature "smart greenhouse" was demonstrated with TOPVs on the roof and windows to harvest solar energy and allow for photosynthesis inside the greenhouse. The height, number of branches, and leaf area of multiple crops grown under the TOPV roof were all slightly higher than for those grown in a greenhouse with a transparent glass roof. This showed that the integration of the TOPVs into the greenhouse roof could protect plants from detrimental UV exposure and promote growth while generating electricity. With these five strategies, the project team showed the strong potential of clean energy greenhouse integrated with TOPVs.

The major advancements of TOPVs through this project can be categorized into new material design for active layers, development of the electrode and interfacial layer, improved stability, and prototyping. Although the initial goal of over 15 percent PCE with 30 percent AVT was not reached, the enhanced performance proved that greenhouses with TOPVs can contribute to both efficient plant photosynthesis and renewable power generation. To identify the benefits of this project as well as future development opportunities, there are remaining challenges in photo-agricultural research. Since agricultural applications require continuous outdoor operation under different climate conditions, a major challenge to resolve is the long-term

operational stability of the TOPV devices. Although the team achieved 1,008 hours of stable operation during this project, the standard for market commercialization will require longer stability, ideally, a decade-long stability along with encapsulation and packaging technology. The ability to weather harsh environments, such as high temperature and humidity, plays an important role in determining the market size of solar panels. The second lesson is that the PCE of the TOPV devices can be dropped when fabricated in large-area modules. Considering the vast agricultural acreage in rural and remote areas, large-area TOPV devices with high performance and mild flexibility are needed. Hence, the development of novel active layers and electrodes with preferable horizontal charge carrier transportation is in demand. The rational design of stable donor and acceptor molecules with preferred transmittance spectra and ideal horizontal charge carrier transportation will greatly advance the commercialization of the TOPVs. TOPVs for agricultural applications holds strong promise for the solar market and have the potential to significantly change modern society. Additional evolutions in this research area are expected to bring this technology to market in the near-term. This project demonstrated that organic photovoltaic technology can enable energy access in remote areas that lack access to reliable grid electricity and can help provide decentralized and off-grid energy solutions. The project also demonstrated that transparent organic photovoltaics can: (1) reduce manufacturing costs; (2) be integrated into urban planning; and (3) provide energy independence.

The outcomes of the project are aligned with California's clean energy and climate goals. As shown over the course of the project, the comparable growth of plants in model greenhouses under TOPV roofs demonstrated that clean electrification in agriculture is possible in California, which has nearly 80,000 farms and ranches (California Ag Today, 2013). Each plant requires a different amount of sunlight conditions and greenhouses with TOPVs can provide suitable sunlight conditions for each crop by tuning light absorption on the solar panels. Along with efficient crop harvesting, TOPV-equipped greenhouses can generate electricity with 13 percent conversion efficiency. It is expected that a typical single solar panel can generate as high as 0.7 kWh per square meter over the course of one day. Installing a solar panel system in currently unused greenhouse roof space would produce meaningful renewable electricity generation in California where energy is at the forefront of agriculture issues. Agriculture in California consumes nearly 8 percent of the state's energy (The Earth Institute, 2008). Recently, under new climate bills (including AB 1279 by Assemblymembers Al Muratsuchi (D-Torrance) and Cristina Garcia (D-Bell Gardens)), clean energy policies in California aim to cut emissions by 85 percent, reduce fossil fuel consumption by 86 percent, and achieve net zero carbon pollution by no later than 2045. Electrifying agriculture using TOPV greenhouses would not only contribute to the efforts in California's energy and climate plans, but also decouple energy dependency from fossil fuels. The periodic spikes in oil and other energy prices highlight the costs of energy-connected agricultural inputs such as fertilizer, electricity, and fuels for trucks and tractors. Therefore, it is necessary to reduce the energy dependency of fossil fuels in the agricultural sector. It is believed that this alternative energy source could help relieve the interconnected concerns of agricultural energy and change the energy relationship for California's agricultural economy.

References

Akira, Yano and Marco Cossu. 2019. "Energy sustainable greenhouse crop cultivation using photovoltaic technologies." *Renew. Sust. Energy Rev*, no. 109: 116.

California Ag Today. 2013. Facts about California Agriculture. Available at: https://californiaagtoday.com/facts-about-california-agriculture/.

California Ag Water Stewardship Initiative (CAWSI). n.d. Available at: https://agwaterstewards.org/practices/water_energy.

Chang, Sheng-Yung, Pei Cheng, Gang Li, and Yang Yang. 2018. "Transparent polymer photovoltaics for solar energy harvesting and beyond." *Joule,* no. 2: 1039.

Chen, Wangqiao and Qichun Zhang. 2017. "Recent progress in non-fullerene small molecule acceptors in organic solar cells." *J. Mater. Chem. C.*, no. 5: 1275.

Cheng, Hao-Wen, Yepin Zhao, and Yang Yang. 2022. "Toward high-performance semitransparent organic photovoltaics with narrow-bandgap donors and non-fullerene acceptors." *Adv. Energy Mater.*, no. 12: 2102908.

Cheng, Pei and Yang Yang. 2020. "Narrowing the Band Gap: The key to high-performance organic photovoltaics." *Acc. Chem. Res.*, no. 53: 1218.

Cheng, Pei, Hao-Cheng Wang, Ran Zheng, Yuan Zhu, Shuixing Dai, Zeyuan Li, Chung-Hao Chen, Yepin Zhao, Rui Wang, Dong Meng, Chenhui Zhu, Kung-Hwa Wei, Xiaowei Zhan, and Yang Yang. 2020. "Enabling high-performance tandem organic photovoltaic cells by balancing the front and rear sub-cells." *Adv. Mater.*, no. 32: 2002315.

Cheng, Pei, Hao-Cheng Wang, Yuan Zhu, Ran Zheng, Tengfei Li, Chung-Hao Chen, Tianyi Huang, Yepin Zhao, Rui Wang, Dong Meng, Yaowen Li, Chenhui Zhu, Kung-Hwa Wei, Xiaowei Zhan, and Yang Yang. 2020. "Transparent hole-transporting frameworks: A unique strategy to design high-performance semitransparent organic photovoltaics." *Adv. Mater.*, no. 32: 2003891.

Liu, Yadi, Ye Yan, Qiang Zhang, Jidong Zhang, Xinhong Yu, and Yanchun Han. 2021. "Increasing the nucleation and growth barrier of a non-fullerene acceptor to achieve bicontinuous pathways in semitransparent ternary polymer solar cells." *J. Mater. Chem. C*, no. 9: 5713.

Meng, Dong, Ran Zheng, Yepin Zhao, Elizabeth Zhang, Letian Dou, and Yang Yang. 2021. "Near-infrared materials: The turning point of organic photovoltaics." *Adv. Mater.*, 2107330.

Meng, Dong, Rui Wang, Janice B. Lin, Jonathan Lee Yang, Selbi Nuryyeva, Yu-Che Lin, Shuai Yuan, Zhao-Kui Wang, Elizabeth Zhang, Chengyi Xiao, Danlei Zhu, Lang Jiang, Yepin Zhao, Zhenxing Li, Chenhui Zhu, Kendall N. Houk, and Yang Yang. 2021. "Chlorinated spiroconjugated fused extended aromatics for multifunctional organic electronics." *Adv. Mater.*, no. 33: 2006120.

The Earth Institute. 2008. *Food Crisis: A Global Emergency*.

Waller, Rebekah, Murat Kacira, Esther Magadley, Meir Teite, and Ibrahim Yehia. 2021. "Semi-transparent organic photovoltaics applied as greenhouse shade for spring and summer tomato production in arid climate." *Agronomy,* no. 11: 1152.

Xie, Yuanpeng, Yunhao Cai, Lei Zhu, Ruoxi Xia, Linglong Ye, Xiang Feng, Hin-Lap Yip, Feng Liu, Guanghao Lu, Songting Tan, and Yanming Sun. 2020. "Fibril network strategy enables high-performance semitransparent organic solar cells." *Adv. Funct. Mater*., no. 30: 2002181.

Zhao, Yepin, Pei Cheng, Hangbo Yang, Minhuan Wang, Dong Meng, Yuan Zhu, Ran Zheng, Tengfei Li, Anni Zhang, Shaun Tan, Tianyi Huang, Jiming Bian, Xiaowei Zhan, Paul S. Weiss, and Yang Yang. 2021. "Towards high-performance semitransparent organic photovoltaics: Dual-functional p-type soft interlayer." *ACS Nano*, no. 16: 1231.

Zhao, Yepin, Yuan Zhu a, Hao-Wen Cheng, Ran Zheng, Dong Meng, and Yang Yang. 2021. "A review on semitransparent solar cells for agricultural application." *Mater. Today Energy*, no. 22: 100852.

Zhao, Yepin, Zongqi Li, Caner Deger, Minhuan Wang, Miroslav Peric, Yanfeng Yin, Dong Meng, Wenxin Yang, Xinyao Wang, Qiyu Xing, Bin Chang, Elizabeth G. Scott, Yifan Zhou, Elizabeth Zhang, Ran Zheng, Jiming Bian, Yantao Shi, Ilhan Yavuz, Kung-Hwa Wei, K. N. Houk, and Yang Yang. 2023. "Achieving sustainability of greenhouses by integrating stable semi-transparent organic photovoltaics." *Nat. Sustain.*, no. 6: 539.

Project Deliverables

The project deliverables include:

1. New IR Absorbing Donors and Acceptors for TOPVs Report
2. Advanced Electrodes for TOPVs Report
3. Advanced Interface Layers for TOPVs Report
4. TOPV Devices Report
5. "Smart Greenhouse" Prototype Development Report
6. Kick-off Meeting Benefits Questionnaire
7. Mid-term Benefits Questionnaire
8. Final Meeting Benefits Questionnaire
9. Initial Fact Sheet
10. Final Project Fact Sheet
11. Final Technology/Knowledge Transfer Report
12. Production Readiness Plan
13. TAC Summary Report
14. Progress Report-July. 2019 to Sep. 2020
15. Progress Report-Oct. 2020 to Dec. 2020
16. Progress Report-Jan. 2021 to Mar. 2021
17. Progress Report-Apr. 2021 to Jun. 2021
18. Progress Report-Jul. 2021 to Sep. 2021
19. Progress Report-Oct. 2021 to Dec. 2021
20. Progress Report-Jan. 2022 to Mar. 2022
21. Progress Report-Apr. 2022 to Jun. 2022
22. Progress Report-Jul. 2022 to Sep. 2022
23. Progress Report-Oct. 2022 to Dec. 2022
24. Progress Report-Jan. 2023 to Mar. 2023
25. Progress Report-Apr. 2023 to Jun. 2023
26. Final Report